FLEXIBLE/STRETCHABLE STRAIN GAUGES BASED ON SINGLE-CRYSTALLINE SILICON FOR BIOMEDICAL APPLICATIONS

BY

ABID AMEEN

THESIS

Submitted in partial fulfillment of the requirements
for the degree of Master of Science in Materials Science and Engineering
in the Graduate College of the
University of Illinois at Urbana-Champaign, 2013

Urbana, Illinois

Adviser:

Professor John A. Rogers

ABSTRACT

Advancement in the semiconductor materials, mechanics and fabrication techniques enable the use of conventional wafer based electronics in unconventional ways via bio-integration. Tissue deformations as a vital sign are conventionally monitored through imaging technologies such as MRI. Strain gauges with equal or greater mechanical compliance are required to measure strains in soft substances, for instance, the human body. This thesis presents tissue-like soft strain gauges through successful integration of metal or silicon nanomembranes on thin flexible and stretchable substrates. Flexible metal strain gauge systems demonstrate high flexibility with low gauge factors, whereas flexible strain gauge systems based on semiconductor materials such as silicon exhibit high gauge factor attributing to their piezoresistive properties on both flexible and stretchable substrates. Innovative applications of high-performance flexible/stretchable strain gauges are demonstrated, including breath monitoring through chest motion detection, ischemia detection through heart motion monitoring, and so on. Tissue-like strain gauges have opened up a new chapter of low cost, high precision *in vivo* bio-strain quantification.

ACKNOWLEDGMENTS

I would like to express my sincere gratitude to Professor John A. Rogers for his support and guidance in my research and preparation of this thesis. I would also like to thank Dr. Nanshu Lu for providing valuable advices and assistance throughout the thesis project. I am also grateful to Sang Min Won, Yun Soung Kim and Lizhi Xu for their assistance in the fabrication process and Dr. Woon-Hong Yeo for his technical support and helpful discussions.

TABLE OF CONTENTS

CHAPTER 1

INTRODUCTION

A wide variety of solid-state sensors for mechanical signals are based on piezoresistive effect where the change in resistance of a transducer indicates the mechanical change of device. The very effect was first introduced by Lord Kelvin in 1856 and used in making strain sensor in 1939 which consist of metal wires on a paper carrier. The piezoresistive effect is rather smaller in metals as compared to Silicon which was first reported by C.S. Smith in 1954 [1]. Due to high sensitivity, good linearity, superior mechanical properties, ease of mass production and integration in standard IC technology, Silicon has widely been used as a suitable material for mechanical sensors and other modern devices [2]. Silicon based electro-mechanical sensors are widely used to measure both motion-related measurands, such as position, displacement, surface roughness, velocity, flow, speed of rotation, and force-related measurands, such as weight, pressure, acceleration, torque, strain, altitude and vibration [3].

Even though many application areas have been investigated, some of the most recent and most sophisticated examples are in unusual format electronics, where semiconductor nanomaterials provide uniform, single crystalline pathways for charge transport between lithographically defined contact electrodes [4–6]. As the dimension of the devices is getting even smaller, there are three critical aspects of mechanics. First, the thickness of the material is much larger than the bending stiffness associated with the film or substrate material [7, 8]. Second, the induced peak strains on the material are linearly dependent on the thickness of the material for known bending radius [7, 8]. A third critical aspect is related with the energy-release rate during

the creation of crack is decreased with thickness of the material [7, 8]. Therefore, by comparison with analogous, wafer based technologies; bonds of nanomaterials are more reliable and robust with one another and with other materials.

In this thesis, I will first introduce an array of piezoresistive strain sensors based on ultrathin single crystalline silicon membranes on a thin plastic substrate which is flexible in nature. Furthermore, in order to conform the strain sensor devices to the curvilinear surfaces of biological tissues stretchable strain sensor have been used. A brief overview of the stretchable materials, fabrication and its application in the biomedical aspects will be discussed.

CHAPTER 2

BASIC PHYSICAL PRINCIPLES

2.1 Metal Strain Gauge

Strain gauges are devices designed to attach to a target object for the purpose of measuring deformations in a precise manner. The most common type of gauge consists of a metal foil which is deposited by e-beam evaporation or by sputtering the target material and then patterned by the wet or dry etching process on a flexible plastic backing. For the strain measurements, the gauge attaches to the object with a suitable adhesive, such as cyanoacrylate. Deformations in the object lead to deformations in the foil, thereby causing its electrical resistance to change. The resistance can be measured as

$$R_o = \frac{\rho_o l}{A} = \frac{\rho_o l}{wt} \tag{1}$$

where ρ_o is the resistivity and $l, w,$ t and A are the length, width, thickness and area of the metal wire, respectively. Applied tensile strain in the device cause the metal lines to be stretched and the relative change in resistance can be written as;

$$\frac{dR}{R_o} = \frac{dl}{l} - \frac{dw}{w} - \frac{dt}{t} + \frac{d\rho}{\rho_o} \tag{2}$$

The negative ratio of the relative contraction strain to the relative extension strain is known as Poisson's ratio and this is a material property.

$$P = -\frac{\varepsilon_w}{\varepsilon_l} = -\frac{dw/w}{dl/l} \tag{3}$$

As $\frac{dw}{w} = \frac{dt}{t}$, equation (2) can be rewritten as;

$$\frac{dR}{R_o} = \varepsilon_l + 2P.\varepsilon_l + \frac{d\rho}{\rho_o} \tag{4}$$

The fractional change in resistance $\frac{dR}{R_o}$ is related to the mechanical strain ε by the gauge factor (GF) as;

$$GF = \frac{dR/R_o}{\varepsilon_l} = 1 + 2P + \frac{d\rho/\rho_o}{\varepsilon_l} \tag{5}$$

The resistivity of the metal lines does not vary with applied strain, therefore, the change in the resistance is only dependent on the geometrical change of the metal lines and above equation can be written as

$$GF = \frac{dR/R_o}{\varepsilon_l} = 1 + 2P \tag{6}$$

The typical value of Poisson's ratio of the metals is smaller than 0.5, and the gauge factor is ~2, indicating a very small piezoresistive effect [3]. However, due to simple structure, metal strain gauges are still very useful in the measurements of force induced strain.

2.2 Silicon Strain Gauge

As discussed in the previous section, the gauge factor of metal is very small; therefore, the applications, where high sensitivity is required for measurements, any material with higher gauge factor should be used. In the 1960s, Smith reported that silicon is a good candidate for these applications due to its high gauge factor of up to 170 for p-type and 135 for n-type [3]. As shown in Eq. (5), the gauge factor of the material depends on two different mechanisms, geometrical change and resistivity change. In metal strain gauge, only the first term contributes to the change of resistance, whereas, in the case semiconductor both terms contribute to the change of resistance. This cause gauge factors to orders of magnitudes larger than those observed in metals.

The strain effect in the resistivity of the silicon can be explained through energy band structure. Energy of the particle in terms of having momentum p and mass m is obtained by

$$E = \frac{p^2}{2m} \tag{7}$$

It can also be expressed in terms of wave-number k ;

$$E = \frac{\hbar^2 k^2}{2m} \tag{8}$$

where h is Planck's constant. An electron in the semiconductor interacts with the periodic lattice which causes two allowed energy bands, conduction band and valance band and a band between these allowed band is obtained which is forbidden energy band as shown in Figure 2.1 [9]. The relationship between E and k only applies for one dimensional lattice as the detailed

band structures in three dimensional k-spaces are rather difficult to construct. In order to understand the three dimensional band structure, it is usual to plot the surfaces of equal energy in three dimensional k-space and assume the crystal to be highly symmetric. Figure 2.2(a) shows the conduction band consist of surfaces of equal energy in three-dimensional k-spaces [10]. It appears that these surfaces are ellipsoids along the main crystal axes and redistribution of carriers among three valleys is the main reason of the piezoresistive effect in n-type silicon.

To explain the carrier redistribution, the mass of the carrier (which are electrons in this case) with known kinetic energy and momentum can be found by differentiating twice and taking the inverse of equation (7).

$$m = \frac{1}{(d^2E / dp^2)} \tag{9}$$

It can also be expressed in terms of wave-number k ;

$$m^* = \frac{h^2}{(4\pi^2 d^2E / dk^2)} \tag{10}$$

The effective mass of the electron in the six minima depends on the motion of the electrons in that energy surface. With electric field along the [100] direction, for example, two-thirds of electrons in energy minima along [001], [00$\bar{1}$], [010], and [0$\bar{1}$0] have a small effective mass and one-third along [100] and [$\bar{1}$00] have a larger mass [10]. The effective masses of electrons in a single valley are anisotropic and hence the mobilities in the valleys are also anisotropic. The conductivity can be written as;

$$\sigma = \frac{2}{3} nq\mu_{\perp} + \frac{1}{3} nq\mu_{\parallel} \tag{11}$$

where σ is the conductivity of silicon, μ is the mobility of the electron, q is electron charge and

n denotes the number of electrons in that valley. Without applying any stress all the valleys degenerate and are equally populated, however, equation (11) no longer applies when strain is applied and carrier redistribution occurred among valleys.

2.3 N-type Silicon

In order to understand the piezoresistive effect in n-type silicon, the effect of the applied stress on the band structure is analyzed. As discussed in the previous section, the interaction between moving electrons and the periodic lattice cause formation of allowed and the forbidden energy bands. When a uniaxial compression stress is applied along the [100] direction, the band edges for the four valleys on [010] and [001] axes goes upward and the band edges on [100] axes goes downward as illustrated in figure 2.2(b). Thus, the electrons are transferred and redistributed from high energy levels to lower energy levels causing more electrons with higher mobilities along [100] direction. The applied electric field in the same direction causes decrease in resistivity and increase in the conductivity.

2.4 P-type Silicon

Energy surfaces for p-type silicon in k-space are more complex and also result in mass changes and holes concentration in valence band contribute to the piezoresistive effect. The valance band of silicon consists of three bands, heavy-hole, light-hole and split-off bands. The heavy-hole and light-hole bands degenerate at band edge k=0 and the split off band is below the band edge, as shown in figure 2.3. The different flatness of heavy- and light-hole results in different effective masses and motilities of holes in those different bands. This difference is greatest in the [111] direction and smaller for the [100] direction [3]. The applied strain removes

the degeneracy and changes the valance band structure. This cause the effective masses of both heavy and light holes to be changed and also redistribution of holes occurred. The effect of this redistribution of holes is large for the [111] direction where the mobility difference between heavy and light hole bands is much more comparable to the [100] direction. The experimental results show that p-type silicon has a positive strain gauge factor, meaning positive or tensile strain along the current direction causes an increase of the resistivity. This indicates that a positive strain cause a band with the lowest mass and highest mobility to lower with respect to the low mobility band so that the holes move to the low mobility band. Figure 2.4 shows the band structure under two different strain conditions: no strain and tensile strain along the [111] direction [11].

2.5 Effect of Doping Concentration

As discussed in the previous sections, the most important property related with the sensitivity of the piezoresistive device is gauge factor. Higher the gauge factor, higher the device sensitivity and vice versa. From the experiment, it has been reported that piezoresistive gauge factor is strongly dependent upon the doping concentration of the silicon (or any semiconductor) as shown in figure 2.4. The experiment gives the relation between impurity concentration and the gauge factor which is inversely proportional. If the material is highly doped, means as the doping concentration is increased, the gauge factor decreases [12]. This phenomenon can also be explained with equation (5) which tells that gauge factor is the relative change of resistance by the applied strain. In highly doped silicon, many electrons occupy the energy state in the conduction band whereas in low doped silicon many electrons stay in the valence band. When the stress is applied, the energy band shifts, and this change solely depends on the magnitude of

the strain. Electrons in higher energy levels move toward the lower energy level until the equilibrium state. If many electrons are available in conduction bands, as in highly doped silicon, the redistribution of the electrons among the valleys can cause the change in the resistance and it is not dependent on the effective mass of the electrons. Therefore, the relative number of replaced electrons is small and thus results in smaller resistance change as well. On the other hand, the relative number of replaced electrons is high in low doped silicon, yielding high gauge factor. This effect can explain the p-type silicon in a similar manner where the change of resistivity is not only depending on the hole redistribution but also on the effective mass of the holes as well [3]. This results in high and low gauge factors for the low doped and highly doped silicon, respectively.

2.6 Effect of Temperature

The other factor which causes the gauge factor to be varied is temperature. It appears that low doped silicon having large gauge factor shows high temperature dependency. In highly doped silicon, many electrons occupy the energy state in the conduction band which is determined by the impurity concentration. Then the temperature does not affect the electron density or, consequently, the gauge factor of the strain gauge. On the other hand, in low doped silicon, the number of electron in the conduction band also depends on the thermally excited electrons in conduction band from the valance band. While the temperature is raised the total number of electrons in the conduction band increases which results in decrease in the gauge factor because the relative change in resistance through electrons redistribution is decreased after applying stress. The temperature dependency of the piezoresistive gauge factor in low doped silicon is shown in figure 2.5 [13, 14].

2.7 Figures

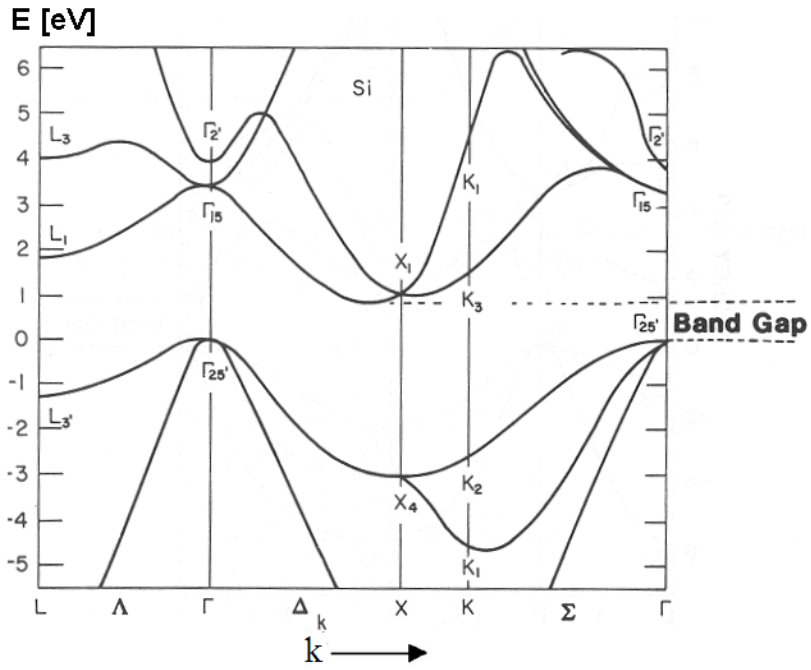

Figure 2.1: Energy-band structure of silicon semiconductor for different k direction where Γ corresponds to k = 0. The gap between the minima of the conduction band and maxima of valance band defines the band gap [9].

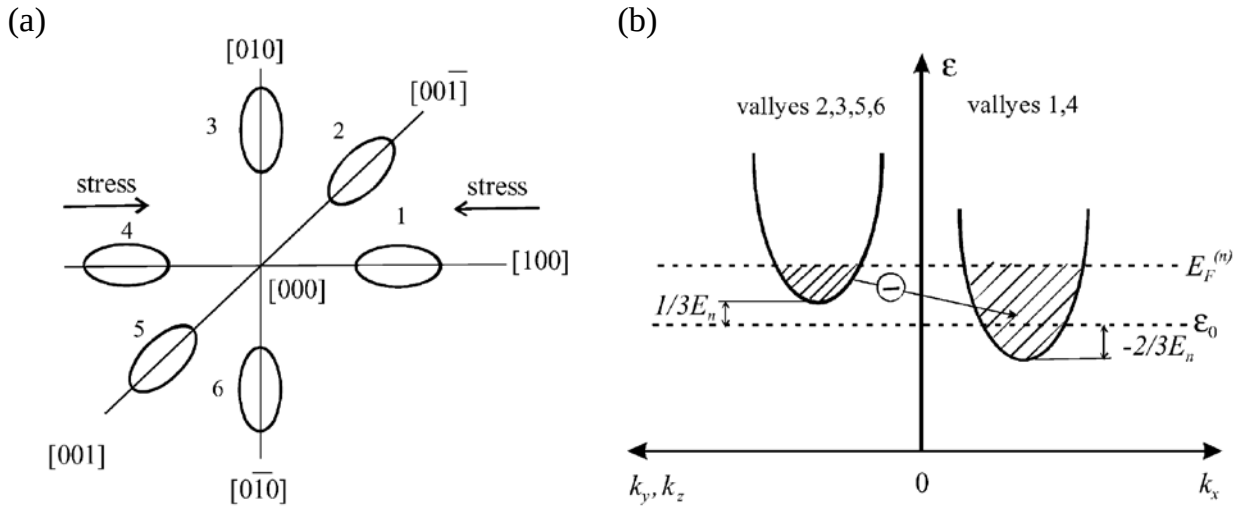

Figure 2.2: (a) Schematic diagram of ellipsoid structures in silicon, referred to as valleys, having equal energy surfaces in three-dimensional k-space for n-type silicon [10]. (b) Schematic diagram of bottom shift of electron valleys under uniaxial stress along the direction [100] [10]. This shift change of energy minima and redistributes the electrons that were originally in the conduction bands along [010] and [001] (referred as 2,3,5,6 valleys) toward the conduction bands along the [100] direction (referred as 1, 4 valleys).

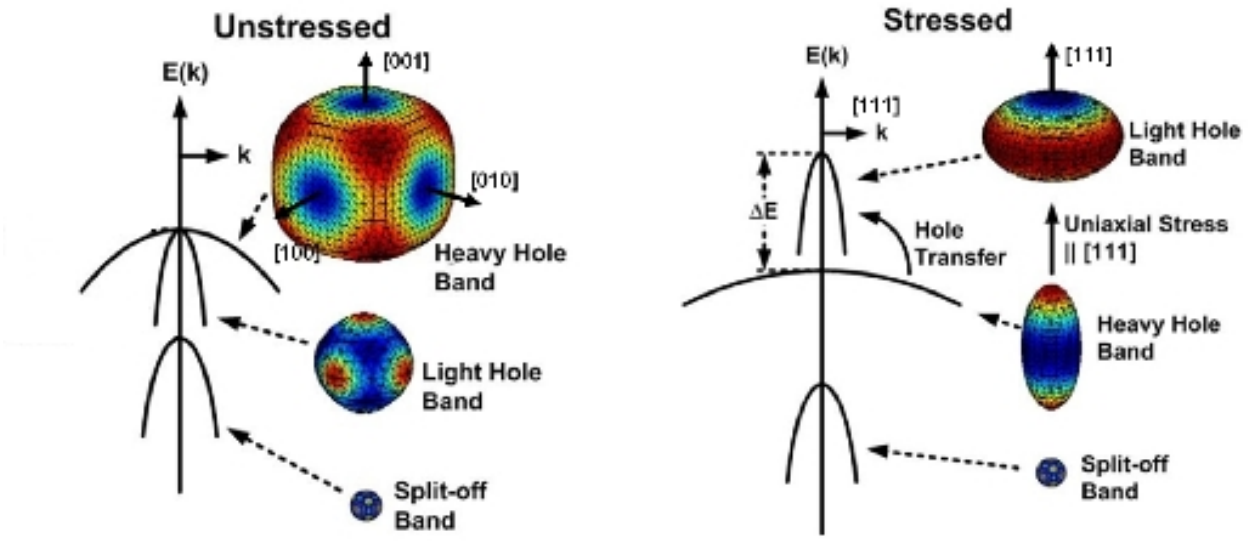

Figure 2.3: Schematic diagram shows the strain effect on the valance band of silicon. Left figure illustrates the E-k diagram and the degeneracy of the heavy- and light-hole bands with split-off bands of Si under no external stress applied. Right figure illustrates the E-k diagram when the stress is applied along [111] direction, the degeneracy is lifted and the light-hole band rises above the heavy-hole band with a band splitting ΔE, causing the hole repopulation from the heavy- to light-hole bands as well as shapes changed [11].

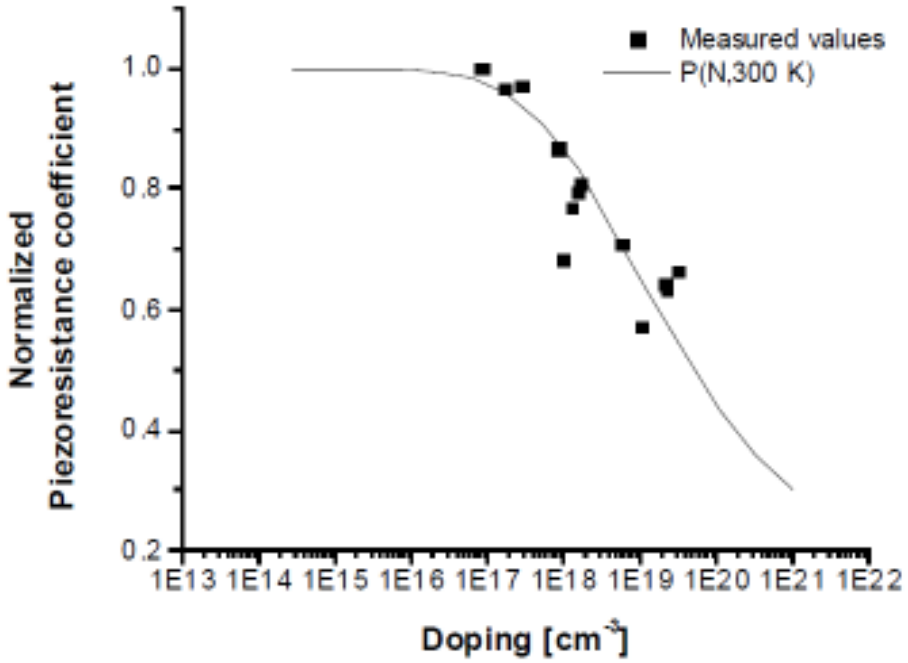

Figure 2.4: The graph shows the normalized piezoresistive gauge factor of silicon strain gauge as a function of the doping concentrations. Increase in doping concentration cause decrease in the gauge factor of the device implies the lower sensitivity of the device [12].

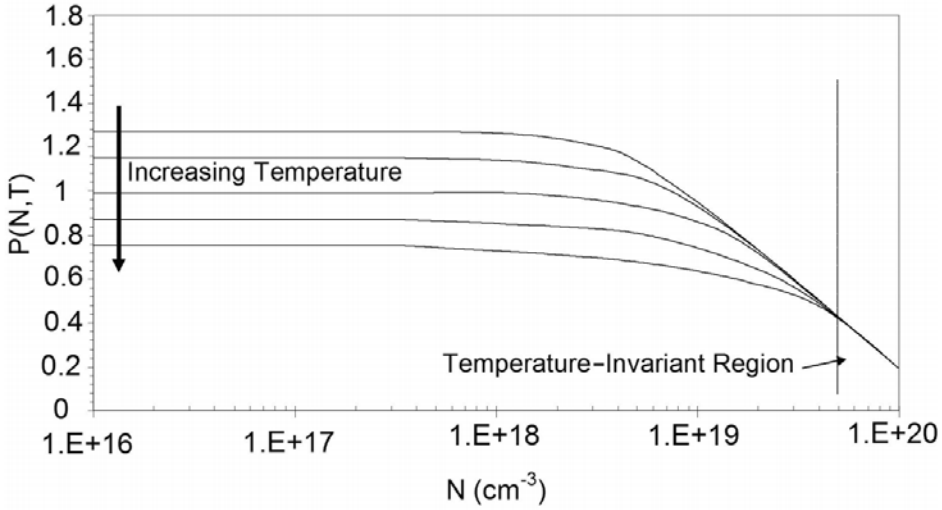

Figure 2.5: Gauge factor of p-type silicon as a function of the temperature. The piezoresistive coefficient P(N,T) is temperature invariant at high doping concentration, and decreased with the increase in the temperature [13, 14].

CHAPTER 3

FLEXIBLE STRAIN SENSOR

3.1 Motivation

As described earlier even though the metal based strain sensors are very simple in fabrication and flexible in nature; their low sensitivity decreases their usage in various applications. For the devices where high sensitivity and signal to noise ratio is needed, a material with better piezoresistive gauge factor need to be considered [3]. Semiconductor material such as silicon has widely been used as suitable material for mechanical sensors and other modern devices due to its high sensitivity, good linearity, superior mechanical properties and ease of integration in standard IC technology [2]. Recently reported highly sensitive, flexible strain sensor array using single crystalline silicon on a thin plastic substrate having the benefits of both metal and semiconductor based strain gauge. The reported technology can be scaled to large-area strain mapping by using Wheatstone bridge (WB) configurations for the sensors and integrating them to multiplexing diodes.

3.2 Process Flow

The fabrication procedure involves transfer printing of doped μs-Si nanomembrane generated from silicon-on-insulator (SOI: Soitec unibond with 300-nm top p-type Si layer with resistivity of 14-22 Ω-cm) onto polyimide (PI) substrate and subsequent processing yields the device structure. Figure 3.1(a) presents simplified process flow and schematic layout of the

transfer printing of μs-Si on the thin kapton film [15].

The process starts by defining high doped regions p and n for making high performance diodes to achieve high ideality factor, and low doping for making Wheatstone bridge element to get high sensitivity because of higher gauge factor. The doping process can be done either through the spin on dopants, diffusion or through ion implantation. First the doping has been done through the spin on dopants and Rapid Thermal Annealer (RTA), however, it is switched towards the solid state doping furnace at 1000^{o}C. The reasons for switching the doping approach to solid state doping are more stable temperature, uniform doping and consistent results among different samples. The doping through the ion implantation is a bit tricky because even the dopants are activated at high temperature; it is hard to see the color contrast of the doping region compared to the undoped region. The higher impurity concentration improves the ohmic contact and temperature independence at the cost of lower piezoresistive factor (i.e. strain sensitivity or gauge factor) as discussed in the previous chapter [3]. In our strain gauge the boron concentration of ~5 x $10^{18}/cm^3$ provides good ohmic contact that yields a linear I-V curve for a μs-Si resistor [15]. The temperature dependence (i.e. temperature coefficient of resistance), at this impurity condition, is reduced by a factor of 5 compared to 1 x $10^{16}/cm^3$ [3, 9, 14], while the strain gauge factor is maintained at ~80% [15]. Then μs-Si printed on the thin polyimide substrate i.e. kepton film spin cast with a thin adhesive layer of polyamic acid (Sigma Aldrich Inc.) followed by the isolation step to make the Wheatstone bridge design on the printed us-Si membrane. Deposition, lithography and wet etching of PECVD-deposited SiO2 interlayer dielectric, e-beam evaporated Cr/Au electrodes and SU-8 encapsulation generate the final device structure as shown in figure 3.1(b). Figure 3.1(c) is an optical image of a strain gauge with Wheatstone bridge configuration on polyimide substrate.

3.3 Experimental Results

Electrical characteristics of the strain sensors arrays such as IV curves for diodes, nominal resistance of strain sensor bridge elements, strain gauge factor by applying tensile strain and switching speed of diodes for multiplexing have been measured. To measure the diode IV characteristics, probe station equipment has been used to apply the voltage range from the -1.0 volt to +1.0 volt. The diode performance is good as the ideality factor is between approximately 1.1 and 1.2 as shown in figure 3.1(e). The ideality factor is a measure of how closely the diode follows the ideal diode equation. The uniformity of the ideality factor results are attributed to good and uniform solid state doping conditions. The piezoresistive gauge factor of the µs-Si resistor of size 20 × 200 μm^2 is measured by applying uniaxial tensile strain longitudinal direction to the thin plastic substrate i.e. Kapton sheet as illustrated in figure 3.1(f). While applying strain, resistance change of the µs-Si resistor with respect to the length change has been investigated to obtain the gauge factor associated with a printed µs-Si resistor on kapton sheet. The resistance of the µs-Si resistor varies linearly with the applied tensile strain, and the reported gauge factor is ~43 as shown in figure 3.1(f) [15].

In order to measure the switching speed of the diode the input signal of different frequencies is applied to the diodes and then the delay is measured between the input signal to the output signal after it passes through the diode as shown in figure 3.2 (a) and (b). The delay between the input and the output signal is 5ns which is very fast response of the diode. Moreover, the operating frequency of the diode is measured by applying different frequency ranges i.e. 100 kHz, 2 MHz and 20 MHz as shown in figure 3.2 (c), (d) and (e) respectively. Most of the multiplexed circuit from national instruments (NI) used the multiplexing of the diodes at range from 1 MHz to 2 MHz. The diodes, which are fabricated in our devices are

showing very good rectification up to 2 MHz frequency range. When the frequency has been increased to 20 MHz which is higher than the response time of the carriers in the diode [16], there is no rectification and shift in phase of the output signal observed. Therefore, if the diode operates within the range of 2 MHz it can perform better for the multiplexing of our strain gauges.

3.4 Application

As mentioned before, for the devices where high sensitivity and signal to noise ratio is needed, semiconductor materials such as silicon with better piezoresistive gauge factor need to be considered. In collaboration with MC-10 Inc., the strain for the golf club is measured. The design and fabrication is similar to the already mentioned flexible strain gauges where the procedure involves transfer printing of doped μs-Si nanomembrane generated from silicon-on-insulator (SOI: Soitec unibond with 300-nm top p-type Si layer with resistivity of 14-22 Ω-cm) onto polyimide (PI) substrate and subsequent processing yields the device structure [15]. In order to measure bi-directional strain, 16 strain gauges with dimension 30μm x 1mm in both longitudinal and transverse direction is made as shown in figure 3.3(a). The sensors are packed with the flexible ACF cable to the external PCB board with mounted connectors for ribbon cables. Ribbon cables are attached to the data acquisition system (DAQ) (with sampling rate at 500 kHz – one sample per 2μ seconds) for real time measurements. The sensor device is integrated onto the Crown surface with thin layer of super glue whereas the PCB and flexible ACF cable is secured with Kapton tape as illustrated in figure 3.3(b). Impact with the real hammer at the face of golf club, strain on the crown is measured as shown in figure 3.3(d). While

applying strain on Kapton sheet, resistance change of the μs-Si resistor with respect to the length change is investigated to obtain the gauge factor associated with a printed μs-Si resistor as shown in figure 3.3(c).

3.5 Figures

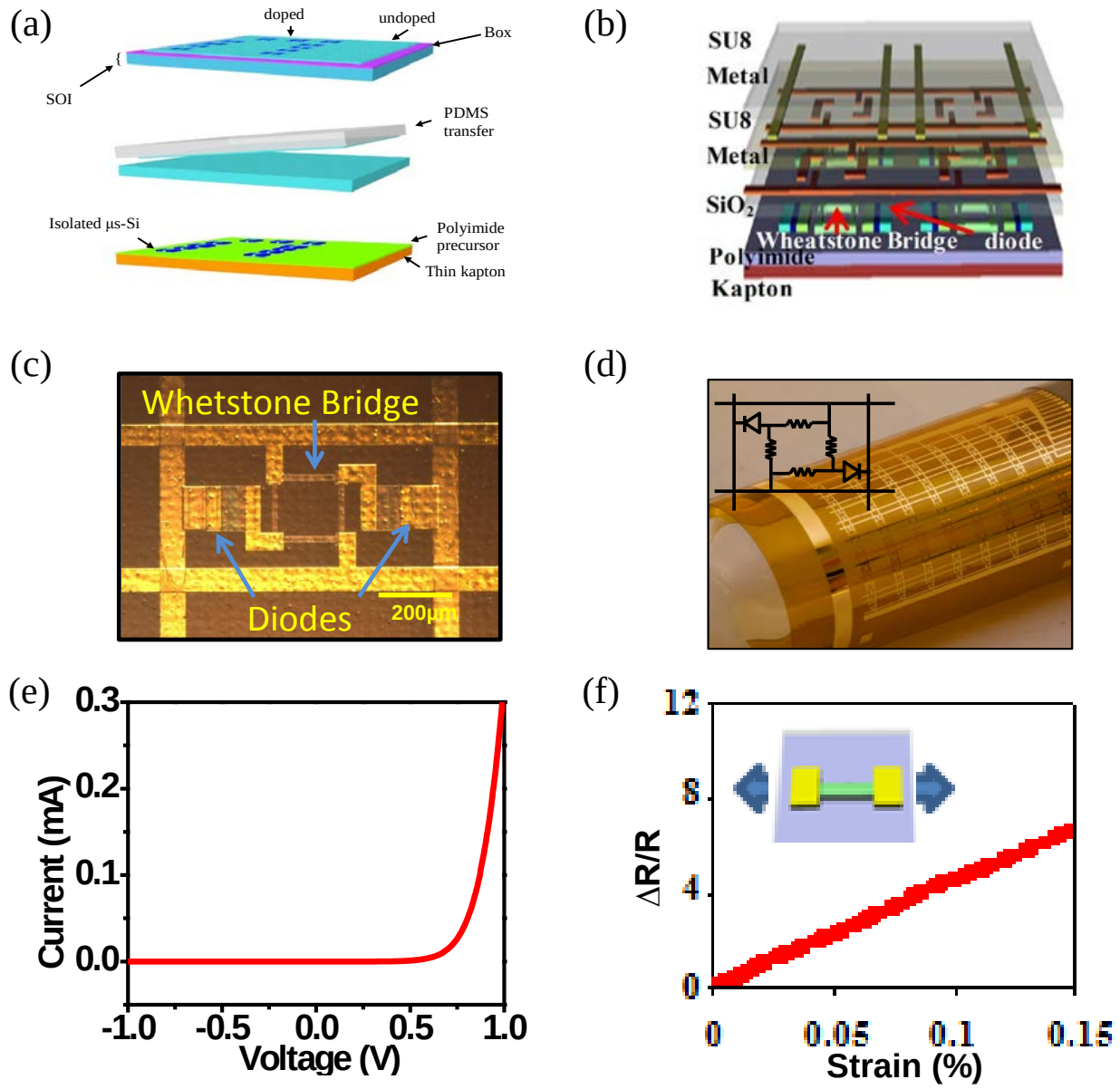

Figure 3.1: (a) Process flow and schematic layout of doped and undoped μs-Si transfer printed on the thin kepton film using PDMS transfer printing technique. (b) Schematic diagram of the cross section of the device, a mapping array of μs-Si strain gauges, with μs-Si p-n diodes for multiplexing [15]. (c) Optical image of top view of a single unit cell of the final device. (d) Optical image of a silicon strain gauge array on a thin plastic substrate (Kapton); the inset on top gives a circuit diagram [15]. (e) Illustrates the Voltage vs. current curves for diodes. (f) The gauge factor of the μs-Si resistor is measured by fractional change in the resistance per applied longitudinal tensile strain [15].

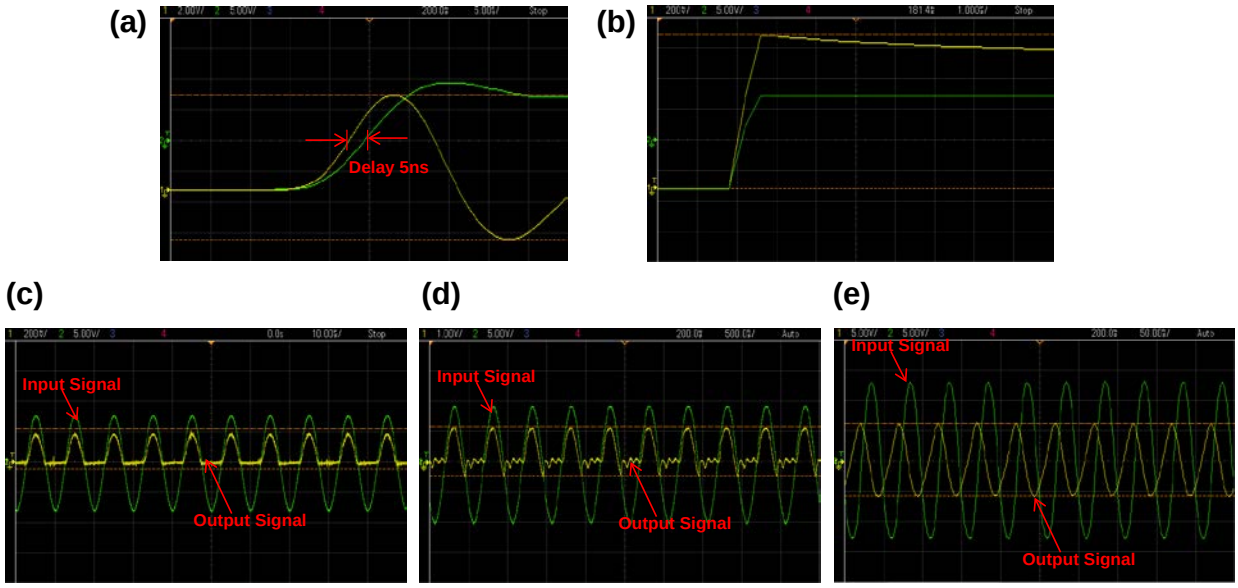

Figure 3.2: (a) and (b) shows delay between the input signal to the output signal after it is passing through the diode which is 5ns. Response of the diode with respect to different frequencies (c) 100 kHz (d) 2 MHz and (e) 20 MHz is elaborated.

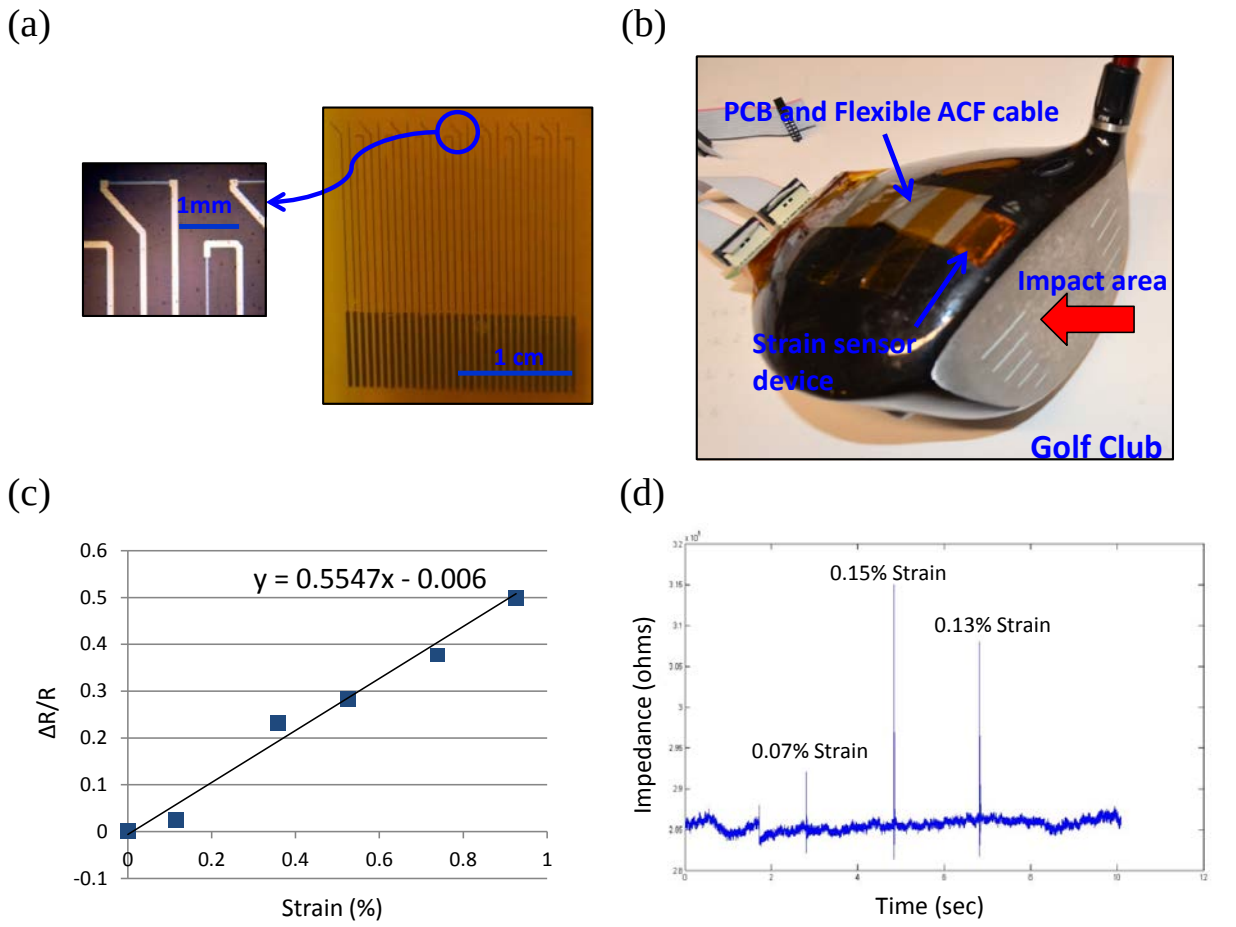

Figure 3.3: (a) Optical image of an array of strain gauges on the thin plastic substrate (Kapton) with the magnified optical image of μs-Si resistor in longitudinal and transverse directions. (b) The sensor device is integrated onto the Golf crown surface with thin layer of super glue whereas the PCB and flexible ACF cable is secured with Kapton tape. The impact area is indicated with red arrow. (c) The gauge factor of the μs-Si resistor is measured by fractional change in the resistance per applied longitudinal tensile strain. (d) Strain on the crown is measured, after the impact at the face of golf club is made with the real hammer.

CHAPTER 4

STRETCHABLE STRAIN SENSOR

4.1 Motivation

Single-crystal inorganic materials, such as silicon or gallium-arsenide in the form of semiconductor wafers are fundamentally rigid and planar [17]. The human body, on contrary, is soft and curvilinear. This diversion between properties hinders the development of devices capable of intimate, conformal integration with biological tissue. The fabrication techniques using unconventional ways with conventional inorganic semiconductor materials have made commendable advancement nowadays. For instance, bio integrated thin, stretchable tissue-like devices that non-invasively integrate with various organs of the body reflecting its mode of deployment, exploits high quality mono-crystalline semiconductor nanomaterials (such as membrane, ribbons) in mechanically optimized layouts on soft-elastomeric, or flexible/stretchable substrates. Transfer printing techniques lays the foundation for the formation of system that allows facile, non-invasive lamination on biological surfaces such as brain, heart and skin [18]. In order to minimize strains in the active materials, neutral-mechanical plane configurations [19, 20] and serpentine geometrical designs [21, 22] are introduced, whereas device encapsulation with another dielectric layer [23, 24] increases the lifetime of the device. Furthermore, advancement in bioresorbable substrates (e.g., silk) ensure close physical contact to soft tissues and avoid adverse long-term effects that are hazardous to human body [25].

4.2 Fabrication

The fabrication steps for stretchable devices including metal layers for interconnections with elastomer substrates and subsequent steps are illustrated in figure 4.1. The fabrication process starts with Si wafer as a bare substrate and it is coated with polymethylmethacrylate (PMMA) as a sacrificial layer of thickness around 100nm. Similar to the fabrication of the flexible strain gauges, transfer printing of doped μs-Si nanomembrane generated from silicon-on-insulator (SOI: Soitec unibond with 300-nm top p-type Si layer with resistivity of 14-22 Ω-cm) onto spin coated polyimide (PI) which is cured in inert atmosphere at 250°C [15]. This PI layer serves as a support layer for the strain gauge devices. Metallization is done through e-beam evaporation and pattern with photolithography process to form interconnects between the devices. For the encapsulation and locating the devices near the neutral mechanical plane (NMP) to avoid the bending effect, another layer of PI with same thickness is spin coated and cured. To define the open mesh structure, patterned reactive ion etching through the entire multilayer stack is done which allows the bottom silicon substrate to be exposed to the atmosphere other than the device region encapsulation. The device is then immersed in an acetone bath that washes away the underlying sacrificial layer of PMMA and the entire mesh is slowly lifted off [26, 27]. Then, with the help of a flat slab of polydimethylsiloxane (PDMS) stamp, using procedures described previously, the whole mesh is picked up and a layer of Cr/SiO^2 is evaporated onto the mesh/PDMS. The target substrate for the stretchable devices such as silicone (Ecoflex 0030, Smooth, Inc.) is exposed to UV-ozone to create reactive –OH groups the surface of which enables bonding between substrate and the device mesh upon physical contact [28]. The final step is the removal of the stamp as shown in figure 4.1(k).

4.3 Figures

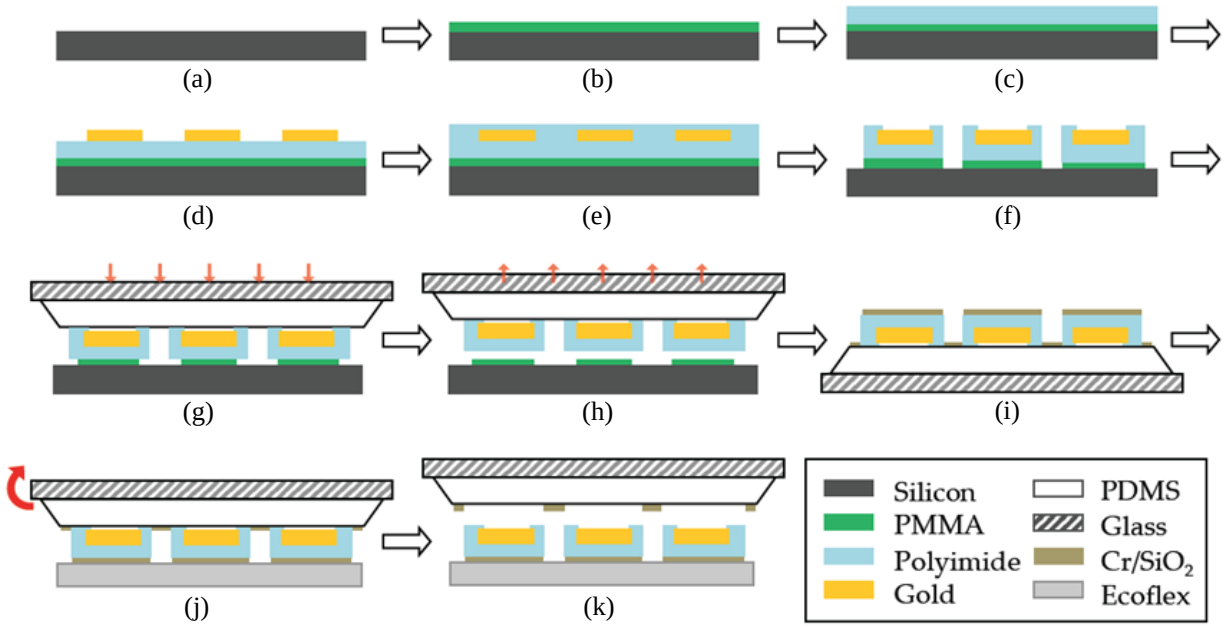

Figure 4.1: Schematic diagrams of the basic fabrication process for stretchable devices. (a) Si substrate; (b) spin coat sacrificial PMMA; (c) spin coat polyimide (PI) precursor which is baked in an inert atmosphere at 250°C; (d) Au evaporation/patterning; (e) spin coat second layer of polyimide (PI) precursor which is again baked in an inert atmosphere at 250°C; (f) Oxygen plasma RIE to etch and patterned PI mesh structure; (g) PMMA undercut in acetone/application of PDMS stamp; (h) devices transferred to PDMS stamp; (i) Cr/SiO2 evaporated onto the back of device; (j) PDMS stamp pressed onto UV exposed Ecoflex; (k) transfer completed with PDMS stamp removal [29].

CHAPTER 5

STRETCHABLE STRAIN SENSOR APPLICATIONS

5.1 Piezoresistive Strain Sensor Web for Cardiac Mapping and Therapy

5.1.1 Motivation:

Irregular electrical activity of the heart is referred to as cardiac arrhythmias commonly atrial fibrillation and ventricular tachycardia, originating in endocardium and then propagating to the epicardial regions [30, 31]. Such anatomical diversity is critical therapeutically. Thus, creating challenges for establishing definitive diagnosis and treatment [30, 32]. Recent advancement in the nanomaterials research introduced techniques that overcame the mismatch between the hard, planar forms of electronics with the soft and curvilinear surfaces of the heart and also avoid the slippage between the interface of the device and the soft tissue. Stretchable sensor webs or sheets, which have ultra-low modulus, integrate with the skin, even on highly irregular, wrinkled regions rendering equivalent mechanical properties that are matched to epidermis [25, 33].

5.1.2 Result and Discussion

A thin (~300μm) soft (Young's modulus ~60 kPa) sheet of silicone (Ecoflex 0030) used as a substrate material for the strain sensor devices which can spatially map mechanical strain distributions, and measure mechanical contractions of the heart and shifts in heart rate during sinus and arrhythmic rhythm [33]. Different kind of strain sensors such as metal wires, Si plates

and mercury-in-rubber structures, have been used for monitoring strain in various parts of the body [34-36], however, none of them is used to measure the characteristics of epicardial applications. Ultrathin Si nanomembrane (NM) generated from silicon-on-insulator as described before configured into piezoresistors as narrow strips in rosettes with longitudinal, diagonal, and transverse orientations as shown in figure 5.1 (a) and (b) incorporated into the sheet of ~0.3mm thick silicone substrate finalizes the fabrication illustrated in figure 5.1(c). The gauge factor is determined by applying uniaxial tensile strain on the sheet as shown in figure 5.2(a). The effective gauge factor is defined as $GF = GF_{Si} \times \varepsilon_g/\varepsilon_a$, where $GF_{Si} = 100$ is the intrinsic gauge factor of single crystalline, ε_g is the average strain in the gauge, and ε_a is the applied strain. Analytical value of the gauge factor (GF) is obtained through mechanical modeling as:

$$GF = GF_{Si}\left[1+\frac{5(EA)_g}{\pi E_{silicone}L_g^2}g_2\left(\frac{w_g}{L_g}\nu_{silicon}\right)\right]^{-1} \tag{12}$$

where $(EA)_g$, L_g, and w_g are the tensile stiffness, length, and width of the gauge, respectively; $E_{silicone}$ and $\nu_{silicone}$ are the Young's modulus and Poisson's ratio of the silicone; and the function g_2 is determined analytically [33]. Using experimental data of $(EA)_g$= 1.6N, $E_{silicone}$= 200kPa, $\nu_{silicone}$ = 0.48, Lg = 0.48mm, w_g = 80μm, equation (12) gives GF = 0.22, which agrees well with effective GF of 0.23 measured in experiments [33]. This value is much smaller than GF_{Si} due to the enormous elastic mismatch between Si nanomembrane resistor and the silicone substrate [37]. The transverse gauge experiences compression causing the decrease in resistance that results from the Poisson effect, whereas, the diagonal gauge does not deform significantly; its response is, therefore, negligible as illustrated in figure 5.2(a). To validate the results quantitatively, finite element analysis (FEA) is used as shown in figure 5.1(d). A silicone sheet

with strain rosettes is stretched along direction 2 (ε_{22}) by 10%. Contour plots of longitudinal strain in $\varepsilon_{22}$of silicone substrate and Si NMs appear in figure 5.1(d), Left and Center [33]. The average tensile strain in the longitudinal resistor is only 0.023% when the substrate is stretched by 10%, resulting in GF = 0.23 according to equation (12). Figure 5.1(d), Right shows the contour plots of strains in direction 1 (ε_{11}, i.e., transverse strain) in the Si NMs. The average strain in the transverse resistor is −0.0070% after 10% longitudinal stretch, resulting in a 0.70% decrease in resistance [33]. As shown in figure 5.1(d), Center and Right, strains in the diagonal resistor approach zero (zero resistance change). The strain patterns associated with expansion/contraction of the beating heart is 5%∼15%, depending on the location of the devices on the heart. These results are in accordance with those obtained by MRI [38] and by FEA [39]. Moreover, by comparing the strain results before and after pacing as well as ischemia, alteration in frequency and in the amplitude is observed as illustrated in figure 5.1(e).

To validate surface adhesion of the device with the tissue of the heart, in vitro tests are performed by laminating the silicone-supported stretchable strain gauges on the surface of a chicken breast, as shown figure 5.3(b). When the chicken breast is stretched longitudinally by 20%, the resulting gauge factor (0.25) is almost the same as that of freestanding gauge (0.23) and there is no slippage observed between the tissue and the device even after the chicken breast is stretched beyond its failure strain (20%) as shown in figure 5.3(c). The bending deformations can also result in variable response which is measured by wrapping the stretchable strain gauge sheet around cylinders with various radii figure 5.3(a). Finally, under cyclical loads with strains of ~30%, reproducibility by devices is noticed as illustrated in figure 5.2(b) [33].

5.2 Piezoresistive Strain Sensors for Fingertip Electronics

5.2.1 Motivation

Electrotactile stimulators and tactile sensors form a bridge between a human operator and a virtual environment, such as therapeutic devices, robotic manipulation, security systems and others [29]. In electrotactile stimulation, the electrical signal is carried via skin, as an artificial sensation of touch, commonly perceived as vibration [40, 41] whereas tactile sensors are meant to measure the pressure created by physical contact. Fabrication strategies and device designs for ultrathin, stretchable silicone-based electronics for integration directly on the fingertips have been reported.

5.2.2 Result and Discussion

The Ecoflex substrates, silicone-elastomer with low modulus (~60 kPa) and large fracture strain (~900%) which is referred to as finger tubes, are obtained with fingers on a plastic model of the hand. The fabrication involves pouring a polymer precursor (Ecoflex) onto a finger of the model and curing at room temperature for 1 h, to create a conformal sheet with ~125μm thickness. Optimal thickness (~500μm with four times repetition) of the sensor substrate is achieved by continuous pouring of precursor onto the sheet and curing for an additional time [29]. Free standing finger-tube substrate for the active devices is made by removing the Ecoflex from the model and cures it for ~2 h at 70^{o}C.

The strain gauge arrays consist of four Si NMs (strips with lateral dimensions of 1 mm × 50 μm and thicknesses of 300 nm) electrically connected by 200 nm thick, 60 μm wide Au traces

patterned in serpentine shapes (radii of curvature ~400 μm) shown in figure 5.4(a) [29]. The FEM calculations, the yellow dashed box in the upper inset, under a uniaxial in-plane strain of 10% shows that the overall strain is mostly accommodated by changes in the shapes of the serpentine interconnects rather than the individual resistor. The Si NM gauges experience strains ($\sim 10^{-3}$) that are ten times lower than the applied strain. The effective gauge factor of the Si NM is experimentally measured by applying uniaxial tensile strain which is ~1 [29].

Figure 5.4(c) shows a strain gauge array on a finger-tube located near the knuckle region of the thumb, in straight (I) and bent (II) positions. Upon bending, the gauges experience tensile strain, resulting in an increase in resistance, as shown for three bending cycles in figure 5.4(d). The relative resistance changes suggest that the strain associated with bending reaches ~6%. As expected, side-to-side motions induce no changes (red curve in figure 5.4(c)). Figure 5.4(e) highlights a similar array on a thin sheet of Ecoflex, mounted near the metacarpal region of the thumb. Here, the device adheres to the skin by van der Waals interactions, similar to the mechanisms observed in epidermal electronic systems [42] which will be described in next application. The images in figure 5.4(e) corresponds to the thumb in straight (III) and sideways deflected (VI) positions. The changes in resistance for the two gauges on opposite ends of the 1 × 4 array for three side-to-side cycles of motion appear in figure 5.4(f). For each cycle, the change in resistance of the rightmost gauge indicates compressive strain; the leftmost indicates the corresponding tensile strain. The results suggest that arrays of gauges can be used to identify not only the magnitude but also the type of motion [29].

5.3 Piezoresistive Strain Sensor Sock for Cardiac Mapping and Therapy

5.3.1 Motivation

Heart is a complex, bi-convex lobular organ. Due to its structural complexity, it is difficult to measure its electrical and mechanical activity simultaneously. Advancement in the semiconductor nanomaterials, in terms of mechanics and fabrication techniques, enable the formation of devices that overcome such anatomical diversities. Although, semiconductor material like silicon has rigid and brittle fundamental properties, but, by investigating the mechanics modeling, it can be integrated with the elastomer material like ecoflex and offers responses to a large strain (~100%) from the object [17]. Stretchable strain sensor cardiac sock, made with ecoflex as a substrate material, have ultra-low modulus (~60 kPa) and it integrates with the soft tissue even on extremely un-even surface. Furthermore, it avoids the slippage between the surface of the device and the cardiac tissue rendering the mechanical properties that are in accordance with the epicardial surface.

5.3.2 Result and Discussion

Fabrication of the cardiac sock is similar to the finger tube, described in the previous application. In order to make the ecoflex substrate referred to as epicardial sock, heart model is made using the 3D printer with all parameters in accordance with the original heart of the animal. The fabrication involves pouring a polymer precursor (ecoflex) onto the heart model and curing at room temperature for 1 h, to create a conformal sheet. Optimal thickness of the substrate for the epicardial sock is achieved by continuous pouring of the precursor onto the sheet and curing for an additional time [29]. Free standing epicardial sock substrate, for the

active devices, is made by removing the ecoflex from the model and cure it for ~2 h at 70^{o}C similar to the finger tube. Figure 5.5(c) shows the finite element analysis (FEA) calculations to measure the pressure of the elastomer sock on the heart. The average pressure with different volume expansion of the original size of the sock is shown in figure 5.5(d), indicating different size matching conditions and time dynamic geometry of the heart. Optimizing the pressure distribution of the sock to the heart is very critical so that elastomer sock conform to the surface of the heart and it will not affect the normal rhythm of the heart. The average pressure from the sock applied to the heart, determined by FEA is 272.7Pa which is comparable to the weight of a penny with thickness of 150um of ecoflex sock and 10% expansion in three dimensions.

Ultrathin Si nanomembrane (NM) generated from SOI as described before configured into piezoresistors as narrow strips in rosettes with longitudinal, diagonal, and transverse orientations as shown in figure 5.5(a) and (b). The Si NM gauges experience strain that is much lower than the applied strain, thus, the effective gauge factor of the Si NM is experimentally measured by applying uniaxial tensile strain which is ~0.15 as shown in figure 5.5(f). This value is much smaller than intrinsic gauge factor of Si, due to high elastic mismatch between the Si nanomembrane resistor and that of the substrate as well as due to shape and dimension of the Si resistor. The in vitro experiment is performed by using Langendorff heart preparation in which the heart is removed from the animal's body and perfused in a reverse fashion with a nutrient rich, oxygen solution [44]. Figure 5.5(e) illustrates the silicon strain gauge device mounted on the epicardial surface of the heart. By comparing the strain results before and after pacing as well as inducing ventricular fibrillation achieved by fast pacing, alteration in frequency and amplitude is observed as illustrated in figure 5.5 (g), (h) and (i) respectively.

5.4 Multifunctional Epidermal Electronics Printed Directly on the Skin

5.4.1 Motivation

In modern day clinical diagnostics, health monitoring devices that can be mounted on the human skin are of great interest due to their versatility in noninvasive, physiological diagnostics [43]. Epidermal electronic systems (EES) are based on fully integrated electronics that have soft stretchable forms designed to match the physical properties such as modulus, thickness and areal mass density of the epidermis itself. These devices laminate and adhere directly on the skin, in a conformal manner, via van der Waals forces alone [43]. The resultant effect is that of a robust and non-irritating skin/electrode contact forming the foundation for intimate integration of diverse classes of electronic and sensor technologies directly with the body. Multifunctional EES are capable of measuring electrophysiological (EP) signals, such as electrocardiograms (ECG) and electromyograms (EMG), as well as temperature and mechanical strain shown in figure 5.6(a) [43].

5.4.2 Result and Discussion

The design consists of an open mesh layout formed by interconnected collection of thin, filamentary serpentine (FS) of conductive material such as gold (Au) to provide interconnect between the devices. These designs are meant to provide low effective elastic moduli and large levels of deformability of the overall system, even when the mesh incorporated with Si (brittle and high modulus material) [42]. Figure 5.6(b) provides an image of a representative EES integrated by directly mounted on the forearm with transfer printing technique and then encapsulated with spray-on-bandage. The spray-on-bandage materials have higher modulus

(~85MPa) and lower elongation (~130%) as compared to the silicone substrate polymers, previously mentioned (Ecoflex® 00-30; modulus: 68.9 kPa and elongation: 900%), with very small thickness (~1μm) [43].

Operation of the EES strain sensor is similar to the other applications described above. The induced strains with cyclical bending of a wrist change the resistance of the Si nanomembrane (NM), which is detected and recorded with 60 Hz notch and lowpass (Butterworth) filters as shown in figure 5.6(d). The effective gauge factor (GF) of the Si NM resistor is calculated when uniaxial tensile strain is applied to the FS EES which is ~5 (figure 5.6(c)). Figure 5.6(e) shows, as an example of the multifunctional capabilities, ECG signals and breathing patterns simultaneously monitored using an EES mounted on the chest. The scope of discussion in this report is related to the strain measurement with the movement of the chest associated with breathing as shown in figure 5.6(f) where the relative resistance change over a span of 60 seconds [43].

5.5 Piezoresistive Strain Sensor as a Physically Transient Form of Silicon Electronics

5.5.1 Motivation

A remarkable feature of modern silicon electronics is its ability to remain physically invariant, almost indefinitely for many practical purposes [45]. Here, a silicon-based technology is introduced that offers the opposite behavior: it gradually vanishes over time, in a well-controlled manner. Devices that are 'transient' in this sense create application possibilities that cannot be addressed with conventional electronics, such as active implants that exist for medically useful timeframes, but then completely dissolve and disappear, in whole or in part, via resorption by the body. These devices include medical monitors that fully resorb when implanted into the human body ("bio-resorbable") to avoid adverse long-term effects or environmental monitors that dissolve when exposed to water ("eco-resorbable") to eliminate the need for collection and recovery. The prescribed technology is based on silicon, therefore it can exploit many modern, established aspects of device and circuit design with operational characteristics that can match those of non-transient counterparts formed in the usual way on wafer substrates [45].

5.5.2 Result and Discussion

Figure 5.7(a) provide a demonstration platform for the transient electronics technology, which includes the components ranging from the inductors, capacitors, resistors, diodes, transistors, interconnects and crossovers to the substrate and encapsulation layers disappear completely through reactive dissolution by hydrolysis as illustrated in the time sequence in figure 5.7(b) [45]. This example of transient electronics uses magnesium (Mg) for the conductors,

magnesium oxide (MgO) and silicon dioxide (SiO2) for the dielectrics, single crystalline silicon nanomembrane (Si-NMs) for the semiconductors, and silk (not only water soluble but also enzymatically degradable [25,46]), for the substrate and packaging material. The fabrication involves a combination of transfer printing (Si NMs), physical vapour deposition through fine-line stencil masks (Mg, MgO, SiO2) and solution casting (silk). MgO and Ti are used as adhesion promoters for Mg. A typical transistor described here involves less than ~1 μg of Si, which can be dissolved as $Si(OH)_4$ in as little as 30 μL of water (or bio-fluid) [47]. Furthermore, the reductions in the dimensions of the devices could decrease even further the required amount of Si. For example, the mass of Si in the active region of a modern MOSFET built on an ultrathin silicon-on-insulator (SOI) wafer is ~10 fg, which corresponds to solubility in as little as ~300 fL [48]. A collection of strain sensors based on doped Si NM resistors with Mg serves as contact and interconnection electrodes and MgO as dielectric layers illustrated in figure 5.7(c) [45]. Figure 5.7(d) shows the fractional change in resistance of a representative strain gauge as a function of time during cyclic loading where bending induces tensile (red) and compressive (blue) strains, uniaxially up to ~0.2 % [45].

5.6 Figures

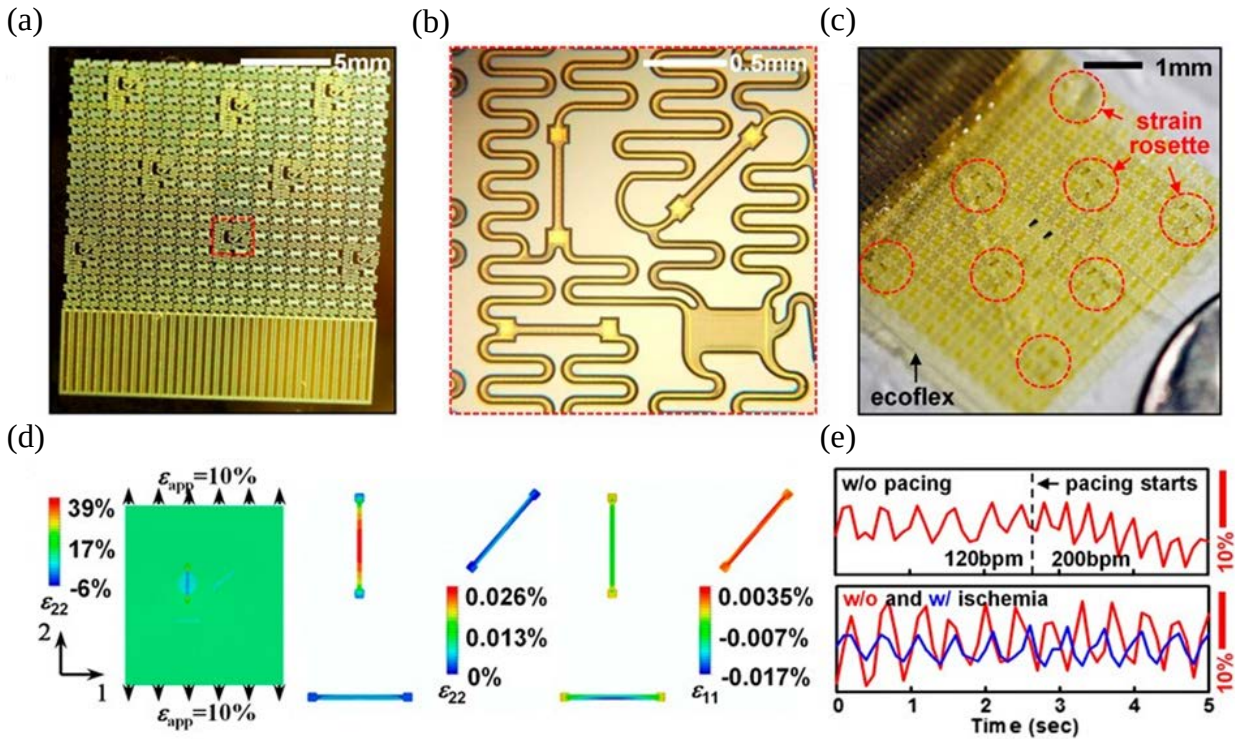

Figure 5.1: Illustration of fabrication, characterization, and modeling of Si nanomembrane for strain gauge webs [33]. (a) Optical image of an array of strain gauges on a silicon wafer [33]. (b) Magnified view of the red dotted box in (a) showing one of the eight strain rosettes with longitudinal, diagonal, and transverse Si NM piezoresistors [33]. (c) Optical image of the final device that consists of an array of eight stretchable strain rosettes on 0.3mm thick silicone substrate (Ecoflex) [33]. (d) Strain distribution in silicone and a Si NM, induced by 10% uniaxial tensile strain. (Left)The longitudinal strains (ε_{22}) in the silicone are uniformly distributed (near 10%) except for the area covered by a longitudinally oriented Si NM; (Center) the ε_{22} in the Si NM are three orders of magnitude smaller than the applied strain; (Right) the transverse strains (ε_{11}) in the transverse Si NM are negative owing to the Poisson's effect in the silicone [33]. (e) In vivo test on the beating rabbit heart determines the strain effect before and after pacing as well as after ischemia [33].

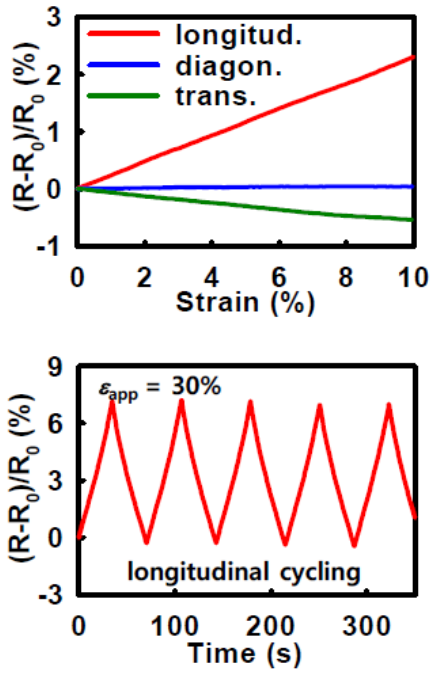

Figure 5.2: (a) Experimental measurement of the change in resistance as a function of uniaxial tensile strain for longitudinal, diagonal and transverse resistors [33]. The gauge factor of the longitudinal resistor is measured as 0.23. (b) Response of a longitudinal strain gauge under cyclic uniaxial stretching, up to 30% [33].

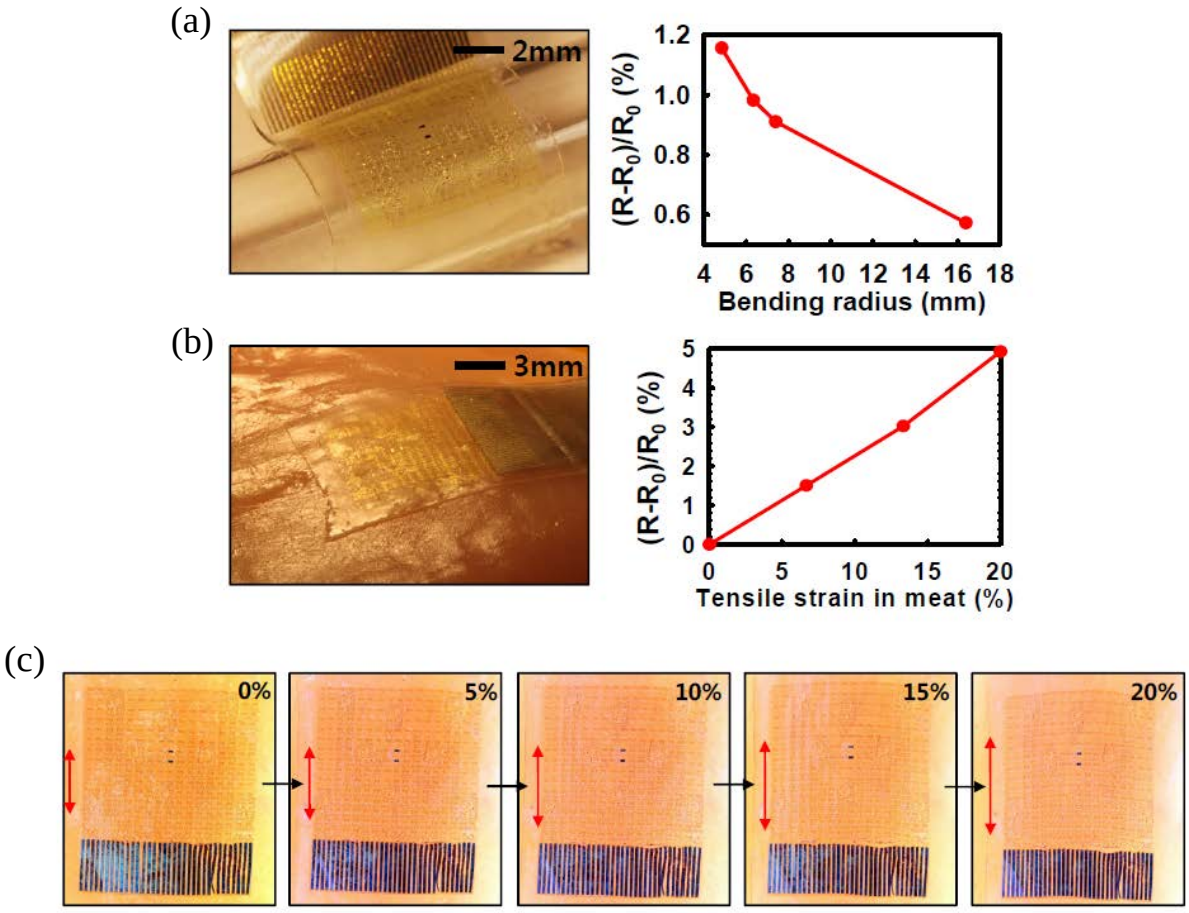

Figure 5.3: (a) Bending tests of the strain gauges measured by wrapping the stretchable strain gauge sheet around cylinders with various radii [33]. (c) Strain gauge web laminated on the raw chicken breast meat under uniaxial tension and gauge factor is determined; which has almost the same value as that of the freestanding gauge [33]. (C) In vitro stretching experiment on the chicken to validate surface adhesion of the device with the tissue of the heart. No slippage occurred as the applied strain is increased up to ~20% [33].

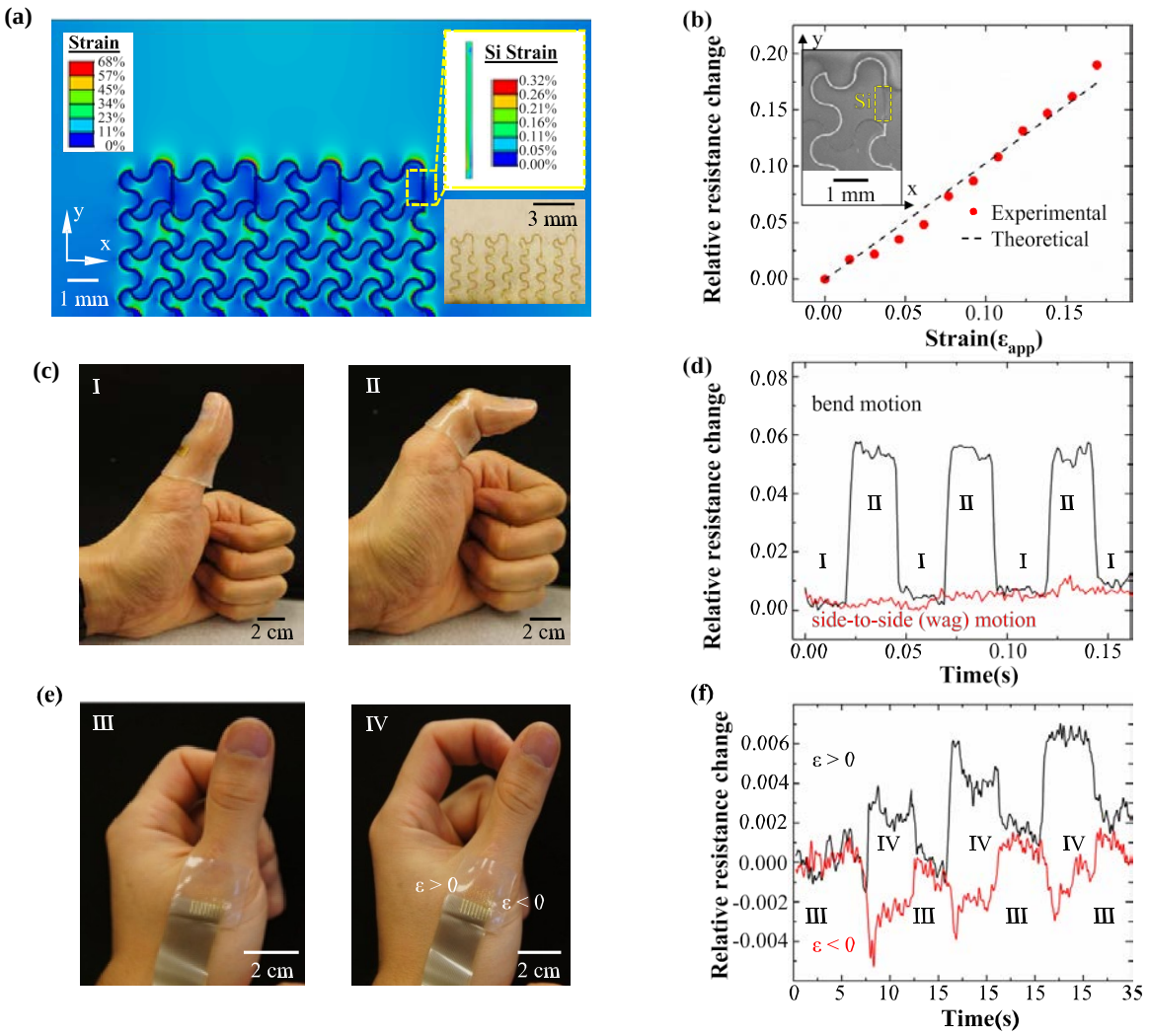

Figure 5.4: Finger motion detection with arrays of stretchable Si nanomembrane (NM) strain gauges [29]. (a) FEM results of the maximum principal strain for a 1 × 4 array of gauges (straight, vertical structures near the top of the serpentine interconnect mesh) due to an overall 10% strain applied along the longitudinal (y) direction. The upper inset shows the strains in the gauge highlighted by the yellow dashed box. The lower inset provides an optical image of a fabricated device with a layout that matches that of the FEM results [29]. (b) Experimentally measured and analytically calculated changes in resistance for a representative Si NM strain gauge as a function of applied strain along the longitudinal direction. The inset provides an SEM image of a portion of the device, with the Si NM gauge located in the dashed box [29]. (c) Images of a strain gauge array on a finger-tube mounted on the thumb, in straight (I) and bent (II) positions [29]. (d) Change in resistance of a representative gauge during three bending cycles (black) and side-to-side motion (red) [29]. (e) Images of a strain gauge array on a thin, elastomeric sheet laminated onto the metacarpal region of the thumb in straight (III) and sideways deflected (IV) positions [29]. (f) Change in resistance of gauges at two ends of the array during three cycles of side-to-side motion [29].

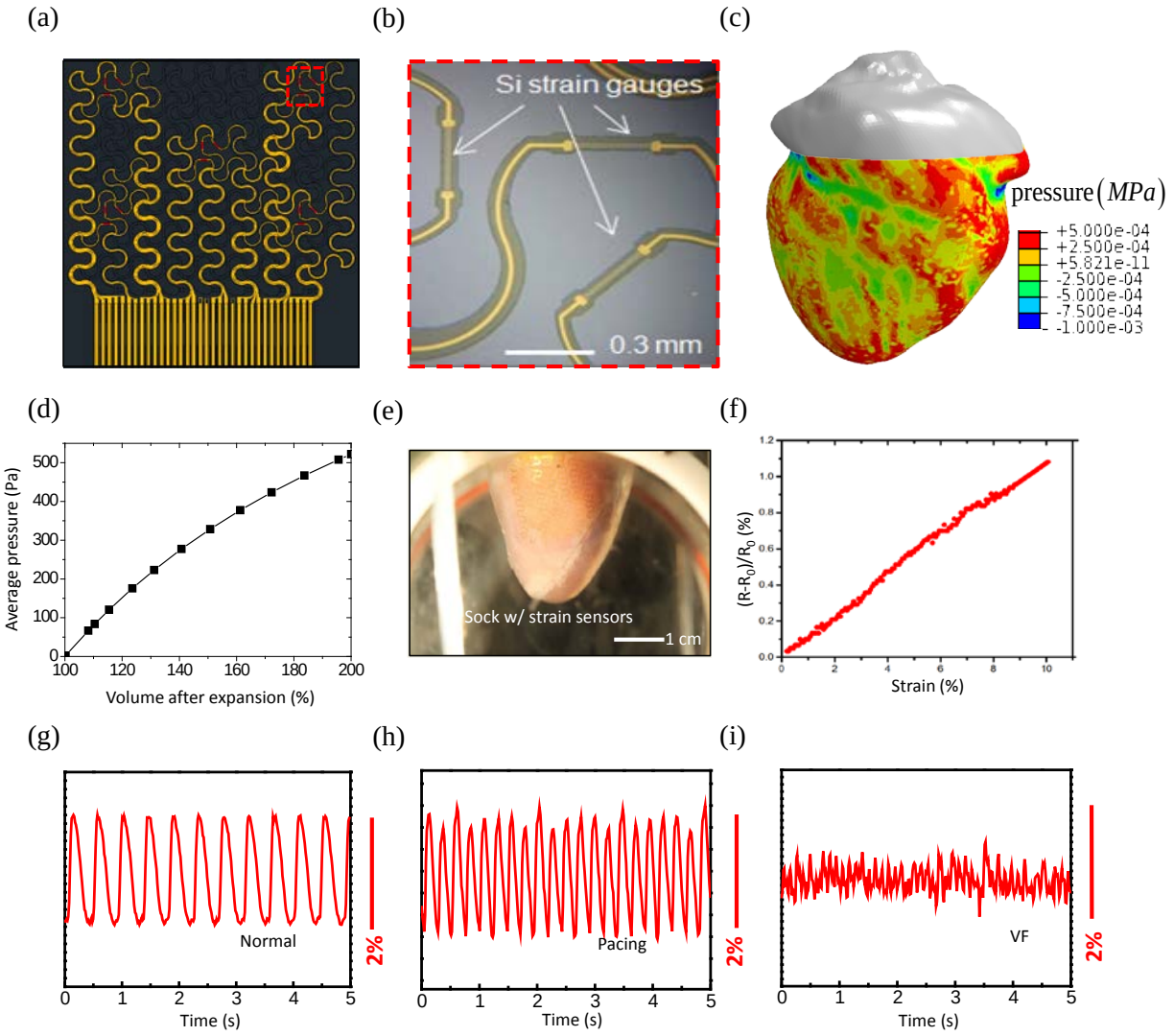

Figure 5.5: Illustration of fabrication, characterization, and modeling of silicone based elastomer (ecoflex) cardiac sock for Si strain gauge. (a) Schematic illustration of a strain gauge array with serpentine mesh interconnects. (b) Optical image of magnified view of the red dotted box in (a) showing one of the five strain rosettes with longitudinal, diagonal, and transverse Si NM piezoresistors. (c) FEA results of pressure distribution of the sock to the heart. (d) Illustration of the average pressure with different volume expansion of the original size of the sock, indicating different size matching conditions and time dynamic geometry of the heart. (e) Illustrates the silicon strain gauge device mount on the epicardial surface of the heart. The in vitro experiment is performed by using Langendorff heart preparation. (f) The gauge factor of the longitudinal μs-Si resistor is measured by fractional change in the resistance as a function of uniaxial tensile strain and reported ~0.15. In vitro test on the beating rabbit heart determines the strain effect before pacing (g), after pacing (h) and inducing ventricular fibrillation by fast pacing illustrates respectively.

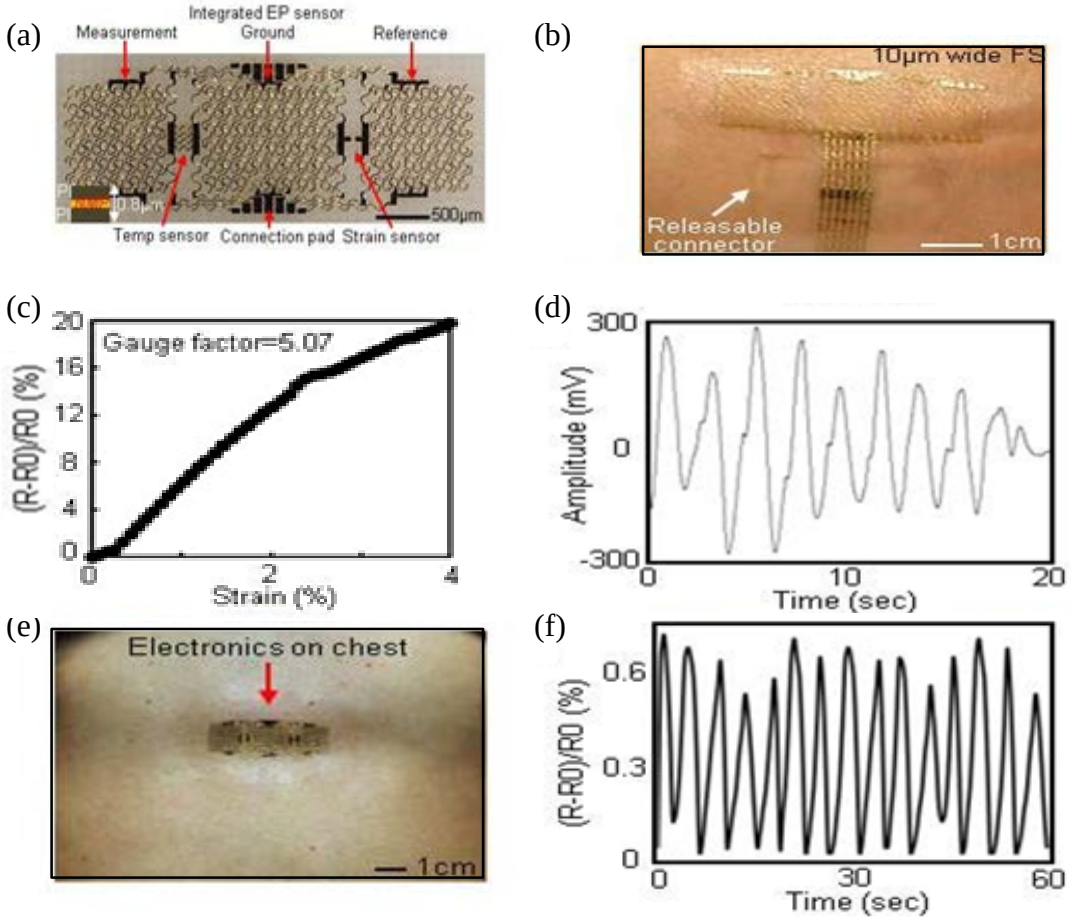

Figure 5.6: Multifunctional epidermal electronic systems (EES), in ultrathin formats, robustly bonded to and encapsulated on the skin and its application for strain sensing on human skin. (a) Optical image of Multifunctional epidermal electronic systems (EES) including an electrophysiological, a temperature and mechanical Si strain sensor [43]. (b) EES on the skin with a releasable connector [43]. (c) The gauge factor of the μs-Si resistor is measured by fractional change in the resistance per applied longitudinal tensile strain and reported ~5 [43]. (d) Measurement of strain by change in the resistance upon bending the wrist inward and outward [43]. (e) Optical image of a multifunctional EES mounted on the chest [43]. (f) Time dependent strain measured during breathing using EES on the chest shown in (e) [43].

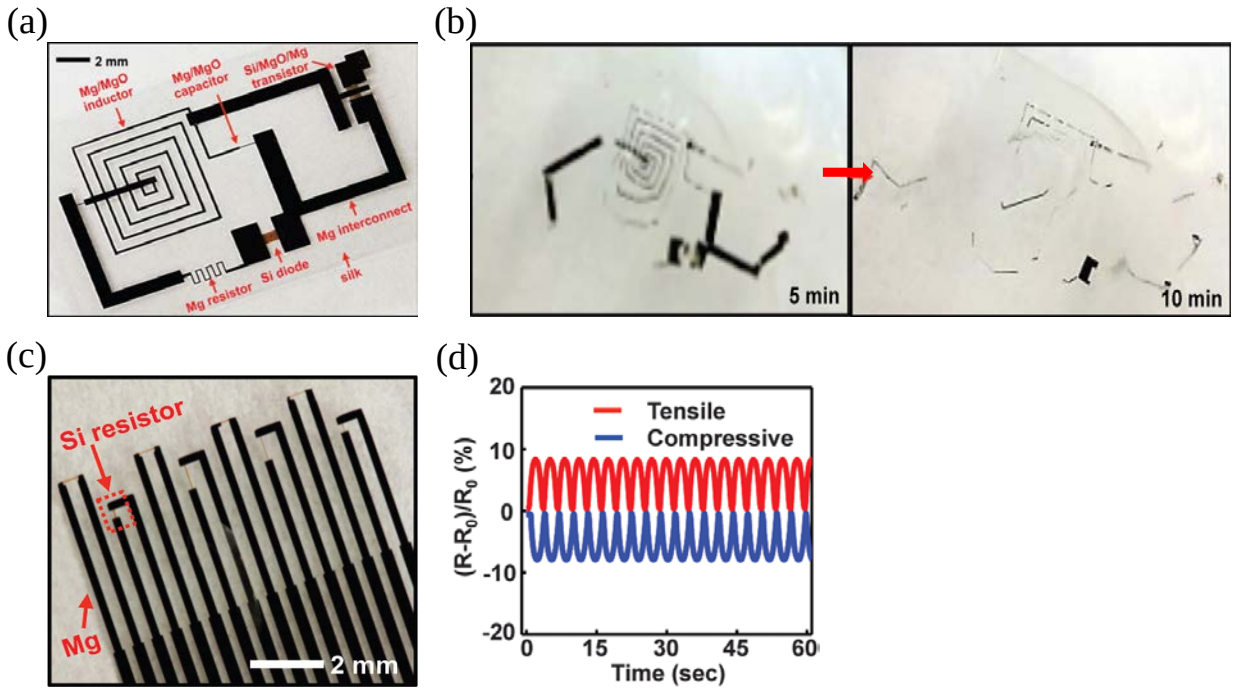

Figure 5.7: Demonstration platform for transient electronics, with key materials and device structures. (a) Image of a transient device that includes, transistor, diode, inductor, capacitor and resistor, with interconnects and interlayer dielectrics, all on a thin silk substrate. (b) Images showing the time sequence of dissolution in DI water of the devices shown in (a). (c) Collection of strain sensors based on Si NM resistors with Mg serves as contact and interconnection electrodes and MgO as dielectric layers. (d) Fractional change in resistance of a representative strain gauge as a function of time during cyclic loading. Bending induces tensile (red) and compressive (blue) strains, uniaxially up to ~0.2 %.

CHAPTER 6

CONCLUSION

As highlighted in this thesis, the advancement in the semiconductor materials, mechanics designs and fabrication techniques established an intimate and minimally invasive interface between conventional wafer-based electronics and soft organisms. In particular, *in vivo*, low-cost strain monitoring requires high-performance strain gauges with compliance comparable to the target tissue. Single-crystalline silicon is ideal for bio-strain sensing due to its highly piezoresistive coefficients, linear and instantaneous strain response, and bio-compatibility. This thesis has discussed the design, fabrication and application of silicon-based flexible/stretchable strain gauge devices Micro-Transfer printing techniques are used to integrate single crystalline silicon strain gauge on thin plastic flexible substrates such as Kapton film and on low modulus stretchable substrates such as PDMS and Ecoflex. The effective gauge factor of the device is highly dependent on substrate property due to substrate-silicon interaction. Ultra-thin, ultra-soft strain gauges have been integrated with animal models and human body for *in vivo* strain monitoring. High cycleability and high repeatiblity have been successfully demonstrated. One of the Future challenges is to construct multiplexed arrays of stretchable strain gauges for high resolution, multi-directional tissue strain mapping.

REFERENCES

[1] C. Smith, “Piezoresistance Effect in Germanium and Silicon,” *Physical Review*, vol. 94, no. 1, pp. 42–49, Apr. 1954.

[2] Y. Kanda, “Piezoresistance effect of silicon,” *Sensors and Actuators A: Physical*, vol. 28, no. 2, pp. 83–91, Jul. 1991.

[3] S. Middelhoek and S. A. Audet, Silicon Sensors. London, UK: Academic Press, 1989

[4] W. Lu and C. M. Lieber, “Nanoelectronics from the bottom up.,” *Nature materials*, vol. 6, no. 11, pp. 841–50, Nov. 2007.

[5] D.-H. Kim, J. Xiao, J. Song, Y. Huang, and J. A. Rogers, “Stretchable, curvilinear electronics based on inorganic materials.,” *Advanced materials (Deerfield Beach, Fla.)*, vol. 22, no. 19, pp. 2108–24, May 2010.

[6] J. A. Rogers, T. Someya, and Y. Huang, “Materials and mechanics for stretchable electronics.,” *Science (New York, N.Y.)*, vol. 327, no. 5973, pp. 1603–7, Mar. 2010.

[7] S.-I. Park, J.-H. Ahn, X. Feng, S. Wang, Y. Huang, and J. A. Rogers, “Theoretical and Experimental Studies of Bending of Inorganic Electronic Materials on Plastic Substrates,” *Advanced Functional Materials*, vol. 18, no. 18, pp. 2673–2684, Sep. 2008.

[8] D.-H. Kim, N. Lu, R. Ghaffari, and J. A. Rogers, “Inorganic semiconductor nanomaterials for flexible and stretchable bio-integrated electronics,” *NPG Asia Materials*, vol. 4, no. 4, p. e15, Apr. 2012.

[9] M. Cohen and T. Bergstresser, “Band Structures and Pseudopotential Form Factors for Fourteen Semiconductors of the Diamond and Zinc-blende Structures,” *Physical Review*, vol. 141, no. 2, pp. 789–796, Jan. 1966.

[10] S. I. Kozlovskiy and I. I. Boiko, “First-order piezoresistance coefficients in silicon crystals,” *Sensors and Actuators A: Physical*, vol. 118, no. 1, pp. 33–43, Jan. 2005.

[11] K. Wu, “Strain effects on the valence band of silicon: Piezoresistance in P-type silicon and mobility enhancement in strained silicon PMOSFET,” Ph.D. dissertation, University of Florida, Gainesvile, FL, 2006.

[12] E. Lund and T. G. Finstad, “Temperature and doping dependency of piezoresistance in p-type silicon,” presented at MRS fall meeting, Boston, MA, 2000.

[13] P. Norton and J. Brandt, “Temperature coefficient of resistance for p- and n-type silicon,” Solid-State Electron., vol. 21, pp. 969-974, 1978.

[14] M. S. B. Zamali and J. J. Talghader, “Stress-mapping sensors for high-power adaptive micro-optics.,” *Applied optics*, vol. 45, no. 7, pp. 1619–26, Mar. 2006.

[15] S. M. Won, H.-S. Kim, N. Lu, D.-G. Kim, C. Del Solar, T. Duenas, A. Ameen, and J. A. Rogers, “Piezoresistive Strain Sensors and Multiplexed Arrays Using Assemblies of Single-Crystalline Silicon Nanoribbons on Plastic Substrates,” *IEEE Transactions on Electron Devices*, vol. 58, no. 11, pp. 4074–4078, Nov. 2011.

[16] R. H. Caverly and G. Hiller, “The frequency-dependent impedance of p-i-n diodes,” *IEEE Transactions on Microwave Theory and Techniques*, vol. 37, no. 4, pp. 787–790, Apr. 1989.

[17] D.-H. Kim, N. Lu, Y. Huang, and J. A. Rogers, “Materials for stretchable electronics in bioinspired and biointegrated devices,” *MRS Bulletin*, vol. 37, no. 03, pp. 226–235.

[18] D.-H. Kim, R. Ghaffari, N. Lu, and J. A. Rogers, “Flexible and stretchable electronics for biointegrated devices.,” *Annual review of biomedical engineering*, vol. 14, pp. 113–28, Jan. 2012.

[19] H. C. Ko, M. P. Stoykovich, J. Song, V. Malyarchuk, W. M. Choi, C.-J. Yu, J. B. Geddes, J. Xiao, S. Wang, Y. Huang, and J. A. Rogers, “A hemispherical electronic eye camera based on compressible silicon optoelectronics.,” *Nature*, vol. 454, no. 7205, pp. 748–53, Aug. 2008.

[20] I. Jung, J. Xiao, V. Malyarchuk, C. Lu, M. Li, Z. Liu, J. Yoon, Y. Huang, and J. A. Rogers, “Dynamically tunable hemispherical electronic eye camera system with adjustable zoom capability.,” *Proceedings of the National Academy of Sciences of the United States of America*, vol. 108, no. 5, pp. 1788–93, Feb. 2011.

[21] D.-H. Kim, J. Song, W. M. Choi, H.-S. Kim, R.-H. Kim, Z. Liu, Y. Y. Huang, K.-C. Hwang, Y. Zhang, and J. A. Rogers, “Materials and noncoplanar mesh designs for integrated circuits with linear elastic responses to extreme mechanical deformations.,” *Proceedings of the National Academy of Sciences of the United States of America*, vol. 105, no. 48, pp. 18675–80, Dec. 2008.

[22] D.-H. Kim, Z. Liu, Y.-S. Kim, J. Wu, J. Song, H.-S. Kim, Y. Huang, K.-C. Hwang, Y. Zhang, and J. A. Rogers, “Optimized structural designs for stretchable silicon integrated circuits.,” *Small (Weinheim an der Bergstrasse, Germany)*, vol. 5, no. 24, pp. 2841–7, Dec. 2009.

[23] J. Viventi, D.-H. Kim, J. D. Moss, Y.-S. Kim, J. A. Blanco, N. Annetta, A. Hicks, J. Xiao, Y. Huang, D. J. Callans, J. A. Rogers, and B. Litt, “A conformal, bio-interfaced class of silicon electronics for mapping cardiac electrophysiology.,” *Science translational medicine*, vol. 2, no. 24, p. 24ra22, Mar. 2010.

[24] R.-H. Kim, D.-H. Kim, J. Xiao, B. H. Kim, S.-I. Park, B. Panilaitis, R. Ghaffari, J. Yao,

M. Li, Z. Liu, V. Malyarchuk, D. G. Kim, A.-P. Le, R. G. Nuzzo, D. L. Kaplan, F. G. Omenetto, Y. Huang, Z. Kang, and J. A. Rogers, “Waterproof AlInGaP optoelectronics on stretchable substrates with applications in biomedicine and robotics.,” *Nature materials*, vol. 9, no. 11, pp. 929–37, Nov. 2010.

[25] D.-H. Kim, J. Viventi, J. J. Amsden, J. Xiao, L. Vigeland, Y.-S. Kim, J. A. Blanco, B. Panilaitis, E. S. Frechette, D. Contreras, D. L. Kaplan, F. G. Omenetto, Y. Huang, K.-C. Hwang, M. R. Zakin, B. Litt, and J. A. Rogers, “Dissolvable films of silk fibroin for ultrathin conformal bio-integrated electronics.,” *Nature materials*, vol. 9, no. 6, pp. 511–7, Jun. 2010.

[26] M. A. Meitl, Z.-T. Zhu, V. Kumar, K. J. Lee, X. Feng, Y. Y. Huang, I. Adesida, R. G. Nuzzo, and J. A. Rogers, “Transfer printing by kinetic control of adhesion to an elastomeric stamp,” *Nature Materials*, vol. 5, no. 1, pp. 33–38, Dec. 2005.

[27] J. Yu and V. Bulović, “Micropatterning metal electrode of organic light emitting devices using rapid polydimethylsiloxane lift-off,” *Applied Physics Letters*, vol. 91, no. 4, p. 043102, Jul. 2007.

[28] D.-H. Kim, J.-H. Ahn, W. M. Choi, H.-S. Kim, T.-H. Kim, J. Song, Y. Y. Huang, Z. Liu, C. Lu, and J. A. Rogers, “Stretchable and foldable silicon integrated circuits.,” *Science (New York, N.Y.)*, vol. 320, no. 5875, pp. 507–11, Apr. 2008.

[29] M. Ying, A.P. Bonifas, N. Lu, Y. Su, R. Li, H. Cheng, A. Ameen, Y. Huang and J.A Rogers, "Silicon Nanomembranes for Fingertip Electronics," Nanotechnology 23 344004, Mar. 2012.

[30] H. Calkins, J. Brugada, D. L. Packer, R. Cappato, S.-A. Chen, H. J. G. Crijns, R. J. Damiano, D. W. Davies, D. E. Haines, M. Haissaguerre, Y. Iesaka, W. Jackman, P. Jais, H. Kottkamp, K. H. Kuck, B. D. Lindsay, F. E. Marchlinski, P. M. McCarthy, J. L. Mont, F. Morady, K. Nademanee, A. Natale, C. Pappone, E. Prystowsky, A. Raviele, J. N. Ruskin, and R. J. Shemin, “HRS/EHRA/ECAS Expert Consensus Statement on Catheter and Surgical Ablation of Atrial Fibrillation: Recommendations for Personnel, Policy, Procedures and Follow-Up: A report of the Heart Rhythm Society (HRS) Task Force on Catheter and Surgical Ablation of ,” *Europace*, vol. 11, no. 1, pp. 132–132, Nov. 2008.

[31] A. G. Kléber and Y. Rudy, “Basic mechanisms of cardiac impulse propagation and associated arrhythmias.,” *Physiological reviews*, vol. 84, no. 2, pp. 431–88, Apr. 2004.

[32] J. Viventi, D.-H. Kim, L. Vigeland, E. S. Frechette, J. A. Blanco, Y.-S. Kim, A. E. Avrin, V. R. Tiruvadi, S.-W. Hwang, A. C. Vanleer, D. F. Wulsin, K. Davis, C. E. Gelber, L. Palmer, J. Van der Spiegel, J. Wu, J. Xiao, Y. Huang, D. Contreras, J. A. Rogers, and B. Litt, “Flexible, foldable, actively multiplexed, high-density electrode array for mapping brain activity in vivo.,” Nature neuroscience, vol. 14, no. 12, pp. 1599–605, Dec. 2011.

[33] D.-H. Kim, R. Ghaffari, N. Lu, S. Wang, S. P. Lee, H. Keum, R. D’Angelo, L. Klinker, Y.

Su, C. Lu, Y.-S. Kim, A. Ameen, Y. Li, Y. Zhang, B. de Graff, Y.-Y. Hsu, Z. Liu, J. Ruskin, L. Xu, C. Lu, F. G. Omenetto, Y. Huang, M. Mansour, M. J. Slepian, and J. A. Rogers, "Electronic sensor and actuator webs for large-area complex geometry cardiac mapping and therapy.," *Proceedings of the National Academy of Sciences of the United States of America*, vol. 109, no. 49, pp. 19910–5, Dec. 2012.

[34] G. BELL, P. E. NIELSEN, N. A. LASSEN, and B. WOLFSON, "Indirect measurement of systolic blood pressure in the lower limb using a mercury in rubber strain gauge," *Cardiovascular Research*, vol. 7, no. 2, pp. 282–289, Mar. 1973.

[35] E. Y. Chao, K. N. An, L. J. Askew, and B. F. Morrey, "Electrogoniometer for the measurement of human elbow joint rotation.," *Journal of biomechanical engineering*, vol. 102, no. 4, pp. 301–10, Nov. 1980.

[36] K. Rome and F. Cowieson, "A reliability study of the universal goniometer, fluid goniometer, and electrogoniometer for the measurement of ankle dorsiflexion.," *Foot & ankle international. / American Orthopaedic Foot and Ankle Society [and] Swiss Foot and Ankle Society*, vol. 17, no. 1, pp. 28–32, Jan. 1996.

[37] J.-Y. Sun, N. Lu, J. Yoon, K.-H. Oh, Z. Suo, and J. J. Vlassak, "Inorganic islands on a highly stretchable polyimide substrate," *Journal of Materials Research*, vol. 24, no. 11, pp. 3338–3342, Jan. 2011.

[38] I. Haber, D. N. Metaxas, T. Geva, and L. Axel, "Three-dimensional systolic kinematics of the right ventricle.," *American journal of physiology. Heart and circulatory physiology*, vol. 289, no. 5, pp. H1826–33, Nov. 2005.

[39] C. M. Nazzal, L. J. Mulligan, and J. C. Criscione, "Efficient characterization of inhomogeneity in contraction strain pattern.," *Biomechanics and modeling in mechanobiology*, vol. 11, no. 5, pp. 585–93, May 2012.

[40] K. A. Kaczmarek, J. G. Webster, P. Bach-y-Rita, and W. J. Tompkins, "Electrotactile and vibrotactile displays for sensory substitution systems.," *IEEE transactions on bio-medical engineering*, vol. 38, no. 1, pp. 1–16, Jan. 1991.

[41] C. A. Lozano, K. A. Kaczmarek, and M. Santello, "Electrotactile stimulation on the tongue: Intensity perception, discrimination, and cross-modality estimation.," *Somatosensory & motor research*, vol. 26, no. 2, pp. 50–63, Jun. 2009.

[42] D.-H. Kim, N. Lu, R. Ma, Y.-S. Kim, R.-H. Kim, S. Wang, J. Wu, S. M. Won, H. Tao, A. Islam, K. J. Yu, T. Kim, R. Chowdhury, M. Ying, L. Xu, M. Li, H.-J. Chung, H. Keum, M. McCormick, P. Liu, Y.-W. Zhang, F. G. Omenetto, Y. Huang, T. Coleman, and J. A. Rogers, "Epidermal electronics.," *Science (New York, N.Y.)*, vol. 333, no. 6044, pp. 838–43, Aug. 2011.

[43] W.-H. Yeo, Y.-S. Kim, J. Lee, A. Ameen, L. Shi, M. Li, S. Wang, R. Ma, S. H. Jin, Z.

Kang, Y. Huang, and J. A. Rogers, “Multifunctional Epidermal Electronics Printed Directly Onto the Skin.,” *Advanced materials (Deerfield Beach, Fla.)*, Feb. 2013.

[44] Broadley,K.J, “The Langendorff heart preparation—Reappraisal of its role as a research and teaching model for coronary vasoactive drugs,” *Journal of Pharmacological Methods*, vol. 2, no. 2, pp. 143 – 156.

[45] S.-W. Hwang, H. Tao, D.-H. Kim, H. Cheng, J.-K. Song, E. Rill, M. A. Brenckle, B. Panilaitis, S. M. Won, Y.-S. Kim, Y. M. Song, K. J. Yu, A. Ameen, R. Li, Y. Su, M. Yang, D. L. Kaplan, M. R. Zakin, M. J. Slepian, Y. Huang, F. G. Omenetto, and J. A. Rogers, “A physically transient form of silicon electronics.,” Science (New York, N.Y.), vol. 337, no. 6102, pp. 1640–4, Sep. 2012.

[46] Y. Wang, D. D. Rudym, A. Walsh, L. Abrahamsen, H.-J. Kim, H. S. Kim, C. Kirker-Head, and D. L. Kaplan, “In vivo degradation of three-dimensional silk fibroin scaffolds.,” Biomaterials, vol. 29, no. 24–25, pp. 3415–28, Jan. 2008.

[47] R. . Iler, “Effect of adsorbed alumina on the solubility of amorphous silica in water,” Journal of Colloid and Interface Science, vol. 43, no. 2, pp. 399–408, May 1973.

[48] B. S. Haran, A. Kumar, L. Adam, J. Chang, V. Basker, S. Kanakasabapathy, D. Horak, S. Fan, J. Chen, J. Faltermeier, S. Seo, M. Burkhardt, S. Burns, S. Halle, S. Holmes, R. Johnson, E. McLellan, T. M. Levin, Y. Zhu, J. Kuss, A. Ebert, J. Cummings, D. Canaperi, S. Paparao, J. Arnold, T. Sparks, C. S. Koay, T. Kanarsky, S. Schmitz, K. Petrillo, R. H. Kim, J. Demarest, L. F. Edge, H. Jagannathan, M. Smalley, N. Berliner, K. Cheng, D. LaTulipe, C. Koburger, S. Mehta, M. Raymond, M. Colburn, T. Spooner, V. Paruchuri, W. Haensch, D. McHerron, and B. Doris, “22 nm technology compatible fully functional 0.1 μm2 6T-SRAM cell,” in 2008 IEEE International Electron Devices Meeting, 2008, pp. 1–4.

APPENDIX

FABRICATION RECIPES AND PROCEDURE FOR STRAIN SENSOR APPLICATIONS

A.1 Fabrication Recipes and Procedure for Flexible Strain Gauges:

1. Cut SOI wafers ((110), 300nm Si) and clean with acetone and IPA.
2. Form a 900nm layer of SiO_2 by PECVD as p-dope diffusion mask.
3. Pattern diffusion mask:
    a. Vapor priming of HMDS
    b. Pattern photoresist (PR) AZ5214:
        i. Spin coat PR AZ5214 (3000rpm, 30s)
        ii. Pre-bake (110°C, 1min)
        iii. Align mask and expose
        iv. Develop with MIF327
        v. post-bake (110°C, 3min)
    c. Wet etch with buffered oxide etchant (BOE) (NH4F: HF=6:1) for 3 min and remove PR with acetone.
4. p-type doping:
    a. Clean wafers with Piranha (H_2SO_4:H_20_2 3:1) for 10min at 100^oC
    b. RCA 1 Clean (H_2O:NH_4OH:H_2O_2 5:1:1) for 10min at 75^oC
    c. RCA 2 Clean (H_2O:HCl:H_2O_2 5:1:1) for 10min at 75^oC
    d. Place samples to boron doping source furnace at 1000°C for 10min
    e. Etch SiO_2 mask and borosilicate glass completely with HF:Piranha:HF for

1min:1min:30sec

5. Form another 900nm layer of SiO_2 by PECVD as n-dope diffusion mask.
6. Pattern diffusion mask:
    a. Vapor priming of HMDS
    b. Pattern photoresist (PR) AZ5214
    c. Wet etch with buffered oxide etchant (BOE) (NH4F: HF=6:1) for 3 min and remove PR with acetone.
7. n-type doping:
    a. Clean wafers with Piranha (H_2SO_4:H_20_2 3:1) for 10min at 100^oC
    b. RCA 1 Clean (H_2O:NH_4OH:H_2O_2 5:1:1) for 10min at 75^oC
    c. RCA 2 Clean (H_2O:HCl:H_2O_2 5:1:1) for 10min at 75^oC
    d. Place samples to boron doping source furnace at 1000°C for 10min
    e. Etch SiO_2 mask and phosphosilicate glass completely with HF:Piranha:HF for 1min:1min:30sec
8. Create holes (Dot pattern 3μm dia., spacing 30μm) for releasing Si membrane from SOI:
    a. Spin coat PR Shipley S1805 (3000rpm, 30s)
    b. Pre-bake (110°C, 1min)
    c. Align mask and expose
    d. Develop with MIF327
    e. Etch Si with Plasma RIE (50 mtorr, 40 sccm SF_6, 100 W, 1min)
9. Transfer printing Si Membrane from SOI
    a. Undercut oxide layer of SOI by immersing wafers in HF (49%) solution for 15~20min until the Si layer is detached from the substrate

b. Prepare target substrate by laminating Kapton sheet on the glass slide
c. Spin coat polyimide precursor PI (4000rpm, 60s) and partially cure at 150°C for 40sec
d. Pick up the Si film from the SOI wafer with a PDMS stamp
e. Transfer Si to target Si wafer by pressing the stamp into contact with the target wafer and apply force with hands for ~20s
f. Put stamp and target substrate on a hotplate at 110°C and slowly release the stamp when thermal expansion of the stamp is observed
g. Put target wafer (now with Si film) on hotplate at 150°C for another 5min
h. Remove PR with acetone
i. Bake PI in an inert atmosphere at 250°C for 1hr.

10. Isolation to make devices and etch unwanted Si
    a. Spin coat PR Shipley S1805 (3000rpm, 30s)
    b. Pre-bake (110°C, 1min)
    c. Align mask and expose
    d. Develop with MIF327
    e. post-bake (110°C, 3min)
    f. Etch Si with Plasma RIE (50 mtorr, 40 sccm SF_6, 100 W, 1min)
    g. Remove PR with acetone
11. Form the dielectric 150nm layer of SiO_2 by PECVD
12. Pattern the dielectric layer:
    a. Vapor priming of HMDS
    b. Pattern photoresist (PR) AZ5214:

c. Etch SiO_2 with Plasma RIE (50 mtorr, 1.2 sccm O_2 40 sccm CF_4, 100 W, 15min)

d. Wet etch with buffered oxide etchant (BOE) (NH4F: HF=6:1) for ~20sec

e. Remove PR with acetone.

13. 1st Au interconnect layer

a. Deposit Cr (5 nm)/Au (200 nm) with electron beam evaporator.

b. Pattern photoresist (PR) AZ5214

c. Wet etch Au and Cr

d. Strip PR with acetone

14. Dielectric layer between first and second metal

a. Spin coat SU-8 2 (3000 rpm for 30 sec)

b. Pre-bake at 65^{o}C for 3 min

c. Pre-bake at 95^{o}C for 1 min

d. Expose 432 mJ/cm^2 (20 sec)

e. Post-bake at 65^{o}C for 3 min

f. Post-bake at 95^{o}C for 1 min

g. Develop with SU-8 Developer

h. Clean with IPA (not with DI water)

i. Final-bake (150^{o}C, 10 min)

15. 2nd Au interconnect layer

a. Deposit Cr (5 nm)/Au (350 nm or higher) with electron beam evaporator.

b. Pattern photoresist (PR) AZ5214

c. Wet etch Au and Cr

d. Strip PR with acetone

16. Encapsulation with SU-8

a. Spin coat SU-8 2 (3000 rpm for 30 sec)

b. Pre-bake at 65^{o}C for 3 min

c. Pre-bake at 95^{o}C for 1 min

d. Final-bake (150^{o}C, 10 min)

A.2 Fabrication Recipes and Procedure for Stretchable Strain Gauges:

1. Cut SOI wafers ((110), 300nm Si) and clean with acetone and IPA.
2. p-type doping on the whole sample:
    a. Clean sample with Piranha (H_2SO_4:H_20_2 3:1) for 10min at 100^{o}C
    b. RCA 1 Clean (H_2O:NH_4OH:H_2O_2 5:1:1) for 10min at 75^{o}C
    c. RCA 2 Clean (H_2O:HCl:H_2O_2 5:1:1) for 10min at 75^{o}C
    d. Place samples to boron doping source furnace at 1000°C for 10min
    e. Etch SiO_2 mask and borosilicate glass completely with HF:Piranha:HF for 1min:1min:30sec
3. Create holes (Dot pattern 3μm dia., spacing 30μm) for releasing Si membrane from SOI:
    a. Spin coat PR Shipley S1805 (3000rpm, 30s)
    b. Pre-bake (110°C, 1min)
    c. Align mask and expose
    d. Develop with MIF327
    e. Etch Si with Plasma RIE (50 mtorr, 40 sccm SF_6, 100 W, 1min)
4. Transfer printing Si Membrane from SOI
    a. Undercut oxide layer of SOI by immersing wafers in HF (49%) solution for 15~20min until the Si layer is detached from the substrate
    b. Prepare target substrate
        i. Spin coat Si wafer (target substrate) with polymethylmethacrylate (PMMA, 3000rpm, 30s, ~100nm)
        ii. Cure at 180°C for 3min
    c. Spin coat polyimide precursor PI (4000rpm, 60s) and partially cure at 150°C for

40sec

d. Pick up the Si film from the SOI wafer with a PDMS stamp
e. Transfer Si to target Si wafer by pressing the stamp into contact with the target wafer and apply force with hands for ~20s
f. Put stamp and target substrate on a hotplate at 110°C and slowly release the stamp when thermal expansion of the stamp is observed
g. Put target wafer (now with Si film) on hotplate at 150°C for another 5min
h. Remove PR with acetone
i. Bake PI in an inert atmosphere at 250°C for 1hr.

5. Isolation to make Si resistors for strain measurements and etch unwanted Si
    a. Spin coat PR Shipley S1805 (3000rpm, 30s)
    b. Pre-bake (110°C, 1min)
    c. Align mask and expose
    d. Develop with MIF327
    e. post-bake (110°C, 3min)
    f. Etch Si with Plasma RIE (50 mtorr, 40 sccm SF_6, 100 W, 1min)
    g. Remove PR with acetone
6. Au interconnect layer
    a. Deposit Cr (5 nm)/Au (200 nm) with electron beam evaporator.
    b. Pattern photoresist (PR) AZ5214:
        i. Spin coat PR AZ5214 (3000rpm, 30s)
        ii. Pre-bake (110°C, 1min)
        iii. Align mask and expose

iv. Develop with MIF327

v. post-bake (110°C, 3min)

c. Wet etch Au and Cr

d. Remove PR with acetone

7. Final PI encapsulation and etch:

a. Spin coat polyimide precursor (4000rpm, 30s)

b. Prebake on hotplate (150°C, 5min)

c. Bake in an inert atmosphere at 250°C for 1hr for complete curing of PI

d. Spin coat PI with PR AZ4620 (3000rpm, 30s)

e. Pre-bake (110°C, 1min)

f. Align via mask and expose

g. Develop with 3:1 diluted MIF400 (40s).

h. Etch exposed polyimide with March RIE (150W, 300mTorr, 20sccm O2, 20min).

i. Remove PR with acetone

8. Transfer printing on the final elastomer substrate (Ecoflex/PDMS):

a. Immerse device in heated acetone bath (100°C) to undercut PMMA

b. Press PDMS stamp into contact with the device and quickly remove to transfer device onto the stamp

c. Deposit Cr (5 nm)/SiO2 (40 nm) with e-beam evaporator

d. Ultra-violet/ozone(UV-O) treat the target substrate (Ecoflex/PDMS) for 4min

e. Press the PDMS stamp onto Ecoflex and remove stamp slowly